Cell Reports

Article

An isoform of the giant protein titin is a master regulator of human T lymphocyte trafficking

Graphical abstract

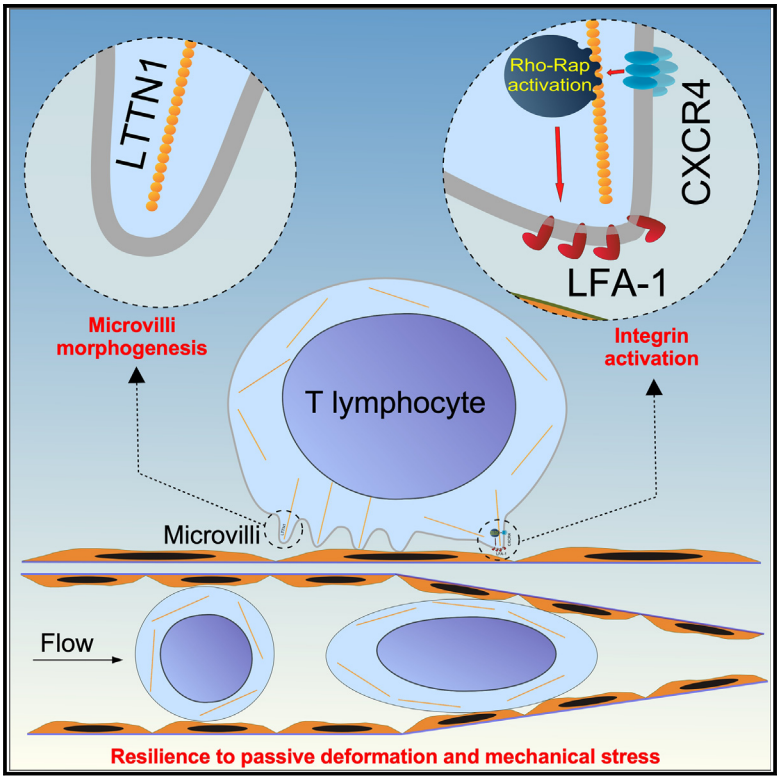

Highlights

- Human T and B lymphocytes express five isoforms of the giant protein TTN
- In T lymphocytes, the LTTN1 isoform regulates the structure of microvilli
- LTTN1 regulates integrin activation and chemotaxis
- LTTN1 controls cell stiffness and deformability and ensures survival in the circulation

Authors

Lara Toffali, Beatrice D'Ulivo, Cinzia Giagulli, ..., Gabriela Constantin, Pierluigi Mauri, Carlo Laudanna

Correspondence

carlo.laudanna@univr.it

In brief

Toffali et al. find that human lymphocytes express five isoforms of TTN. In T lymphocytes, the LTTN1 isoform regulates microvilli structure, integrin activation, and chemotaxis. Moreover, LTTN1 controls cell stiffness and resilience to deformation and ensures survival in the blood stream. LTTN1 is, thus, a central regulator of lymphocyte trafficking.

Toffali et al., 2023, Cell Reports *42*, 112516
May 30, 2023
https://doi.org/10.1016/j.celrep.2023.112516

CellPress

Cell Reports

CellPress
OPEN ACCESS

Article

An isoform of the giant protein titin is a master regulator of human T lymphocyte trafficking

Lara Toffali,[1,8] Beatrice D'Ulivo,[1,8] Cinzia Giagulli,[2,8] Alessio Montresor,[1,3] Elena Zenaro,[1] Massimo Delledonne,[4] Marzia Rossato,[4] Barbara Iadarola,[4] Andrea Sbarbati,[5] Paolo Bernardi,[5] Gabriele Angelini,[1] Barbara Rossi,[1] Nicola Lopez,[1] Wolfgang A. Linke,[6] Andreas Unger,[6] Dario Di Silvestre,[7] Louise Benazzi,[7] Antonella De Palma,[7] Sara Motta,[7] Gabriela Constantin,[1,3] Pierluigi Mauri,[7] and Carlo Laudanna[1,3,9,*]

[1]Department of Medicine, Division of General Pathology, Laboratory of Cell Trafficking and Signal Transduction, University of Verona; 37134 Verona, Veneto, Italy
[2]Department of Molecular and Translational Medicine, University of Brescia; 25123 Brescia, Lombardia, Italy
[3]The Center for Biomedical Computing (CBMC), University of Verona; 37134 Verona, Veneto, Italy
[4]Department of Biotechnology, University of Verona; 37134 Verona, Veneto, Italy
[5]Department of Neurosciences, Biomedicine and Movement Sciences, University of Verona; 37134 Verona, Veneto, Italy
[6]Institute of Physiology II, University of Muenster, and Heart Center, University Medicine; 37075 Göttingen, Germany
[7]Institute of Biomedical Technologies (ITB) CNR; 20090 Milan, Lombardia, Italy
[8]These authors contributed equally
[9]Lead contact
*Correspondence: carlo.laudanna@univr.it
https://doi.org/10.1016/j.celrep.2023.112516

SUMMARY

Response to multiple microenvironmental cues and resilience to mechanical stress are essential features of trafficking leukocytes. Here, we describe unexpected role of titin (TTN), the largest protein encoded by the human genome, in the regulation of mechanisms of lymphocyte trafficking. Human T and B lymphocytes express five TTN isoforms, exhibiting cell-specific expression, distinct localization to plasma membrane microdomains, and different distribution to cytosolic versus nuclear compartments. In T lymphocytes, the LTTN1 isoform governs the morphogenesis of plasma membrane microvilli independently of ERM protein phosphorylation status, thus allowing selectin-mediated capturing and rolling adhesions. Likewise, LTTN1 controls chemokine-triggered integrin activation. Accordingly, LTTN1 mediates rho and rap small GTPases activation, but not actin polymerization. In contrast, chemotaxis is facilitated by LTTN1 degradation. Finally, LTTN1 controls resilience to passive cell deformation and ensures T lymphocyte survival in the blood stream. LTTN1 is, thus, a critical and versatile housekeeping regulator of T lymphocyte trafficking.

INTRODUCTION

During the immune response, leukocytes integrate a multitude of microenvironmental signals,[1] which are concurrently processed by mechanisms of mechano-transduction.[2–12] Circulating leukocytes must also cope with both passive and active cell deformation, respectively generated by the incessant passage across capillary nets[13,14] and, in the course of migration, by the adaption of cell body and nucleus to the small gaps between endothelial cells and within the extracellular matrix three-dimensional (3D) meshwork.[15–17] Therefore, trafficking leukocytes need to simultaneously control pathways of mechano-transduction and the resilience to mechanical stress, suggesting the existence of molecular mechanisms of coordinated regulation of these events. Detergent-resistant membrane domains (DRMs) have provided a structural context to understand the topography and organization of signaling mechanisms,[18–21] and have been widely implicated in many aspects of leukocyte physiology.[22] Consequently, we postulated that DRMs could provide anchoring to proteins that concurrently coordinate mechano-signaling and resilience to mechanical stress in human primary leukocytes.

Here, we show that titin (TTN), the largest protein encoded by the human genome, and the main controller of muscle cell passive stiffness,[23–26] plays a central role in the regulation of T lymphocyte trafficking. Human lymphocytes constitutively express the *TTN* gene. Five TTN isoforms are generated in T and B lymphocytes, encompassing, altogether, the entire *TTN* gene. The three isoforms expressed in T lymphocytes are characterized by different distribution to cytosolic and nuclear compartments, with the two largest isoforms associated with the DRMs. Functional analysis of the T lymphocyte-specific LTTN1 isoform demonstrates its critical regulatory role in every step of T lymphocyte recruitment process. Moreover, LTTN1 protects resting T lymphocytes from the mechanical stress induced by passive cell deformation and, thus, facilitates their survival in the microcirculation. Thus, constitutive expression of the *TTN* gene is critical to the regulation of T lymphocyte trafficking.

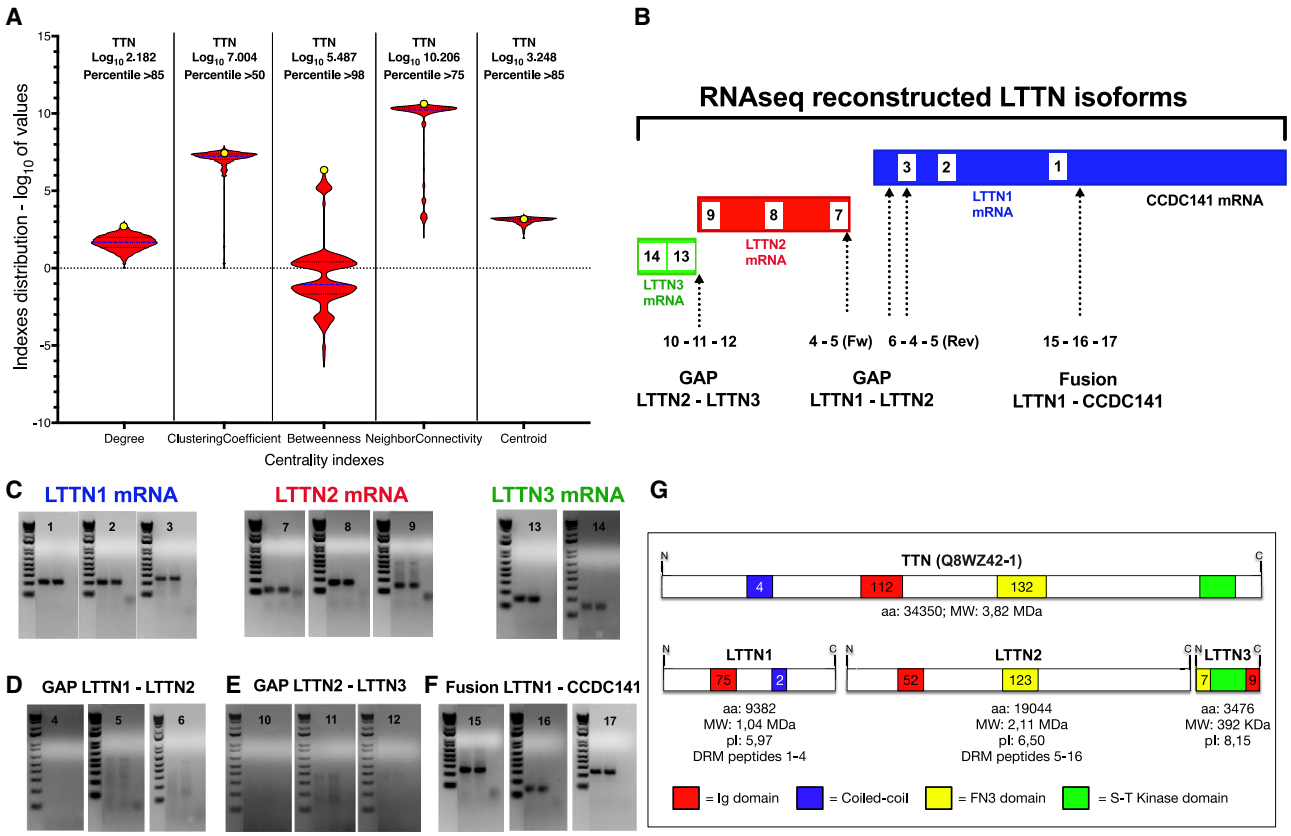

Figure 1. | Transcript expression of TTN isoforms in T lymphocytes

(A) Node centrality analysis of DRM network; shown are violin plots of value distribution of five centrality indexes calculated for every node (protein) in the inferred DRM PPI network. To allow comparison between different centrality indexes, values are plotted as $\log_{10}$. On top, for every centrality index is reported the $\log_{10}$ value of TTN, along with its percentile ranking. In the individual violin plots, TTN is indicated as a yellow circle to show its relative position with respect to median (blue dashed line) and percentiles (black dotted lines). See also Data S1.

(B) Human T lymphocyte-specific *TTN* transcripts reconstructed from RNA-seq data are shown in blue, red, and green. Primers used for PCR validation are indicated by numbers and arrows.

(C) Validation of RNA-seq data for *LTTN1* (primers 1, 2, 3), *LTTN2* (primers 7, 8, 9), and *LTTN3* (primers 13, 14) mRNAs.

(D) Validation of gap between *LTTN1* and *LTTN2* mRNAs (primers 4, 5, 6).

(E) Validation of gap between *LTTN2* and *LTTN3* mRNAs (primers 10, 11, 12).

(F) Validation of upstream fusion between *LTTN1* and *CCDC141* mRNAs (primers 15, 16, 17). One representative experiment of three is shown in (C)–(F); see also Data S2 and Figure S1.

(G) Diagrams of TTN protein isoforms expressed in human T lymphocytes, predicted from the transcripts described in (B) compared with the canonical muscle isoform (UniProt ID Q8WZ42-1). The number of amino acids, MW, isoelectric point (pI), and the MS-identified peptides in DRMs are shown, along with the position and total number of immunoglobulin (red), CC (blue), fibronectin III (yellow), and S/T kinase (green) domains. See also Table S3.

RESULTS

Human lymphocytes express five TTN isoforms

The analysis of DRMs by mass spectrometry (MS) following their isolation from human primary resting T lymphocytes identified 82 proteins, including the giant protein TTN, which ranked eighth (Table S1). MS analysis detected 16 peptides mapping to different TTN regions (Table S2). TTN is a 3,800-kDa spring protein, 1.1 μm in length, composed of ~34,000 amino acid residues, which provides muscle cells passive stiffness. It is by far the largest multi-scaffolding signaling protein encoded by human genome, and the largest isoform comprises 132 fibronectin type III domains, 112 type II immunoglobulin domains, four coiled-coil (CC) domains, and additional spring and kinase domains.[23–26] Protein-protein interaction (PPI) network inference showed that 54 proteins identified in DRMs may establish direct interactions with at least 2,918 protein partners, generating an interactome space of 114,446 interactions (Data S1). In this DRM protein interactome, TTN interacts with 152 proteins, with 98 proteins consistently expressed in human T lymphocytes (Data S1), leading to a T lymphocyte-specific subnetwork of 1,310 binary interactions (Data S1). Computation, for every protein in this DRM interactome, of five centrality indices indicating the possible emergence of modularity[27–31] showed that TTN ranked between the 50th and 98th percentiles, with particularly remarkable scores for the degree (>85th), centroid (>85th), and betweenness (>98th) values (Figure 1A). Overall, the functional, structural, and topological features of TTN make it an ideal

candidate coordinator of mechano-transduction and cell stiffness in human T lymphocytes. The MS data were fully confirmed by RNA sequencing (RNA-seq) analysis, which revealed the expression of 270 exons of the *TTN* gene (Data S2). Importantly, RNA-seq data *de novo* assembly demonstrated the reconstruction of three distinct transcripts for the *TTN* gene, clearly separated by two gaps showing no sequencing reads spanning across and thus suggesting that T lymphocytes express three TTN isoforms (Figure 1B). These findings were verified and confirmed by PCR, which showed amplification of the reconstrued transcripts but no amplification of the regions predicted as gaps (Figures 1C, 1D, 1E, S1A, and S1B), confirming that human primary T lymphocytes express three TTN isoforms, each mapping to different segments of the *TTN* cDNA consensus sequence. The isoforms were designated LTTN1 (118 exons), LTTN2 (137 exons), and LTTN3 (15 exons). Interestingly, the RNA-seq and PCR data indicated that the *LTTN1* transcript was fused to that of the upstream gene *CCDC141* (Figures 1F and S1C; Data S2), although not in frame, suggesting the translation into two separate proteins. Identification of isoforms' aminoacidic sequence encoded by the RNA-seq-reconstructed transcripts by using BLASTx predicted that LTTN1 consists of 9,382 amino acids with a molecular weight (MW) of 1.04 MDa, LTTN2 consists of 19,044 amino acids with an MW of 2.11 MDa, and LTTN3 consists of 3,476 amino acids with an MW of 392 kDa (Figure 1G). BLASTp alignment of the predicted aminoacidic sequences with canonical TTN revealed the presence in the three isoforms of multiple protein domains regulating PPI, signal transduction, and the response to mechanical stress (Figure 1G). Note that we were able to assign MS-detected peptides to LTTN1 (peptides 1–4) and LTTN2 (peptides 5–16) but not to LTTN3, suggesting that LTTN1 and LTTN2, but not LTTN3, are associated with DRMs (Table S3).

The expression of the three TTN isoforms in T lymphocytes was confirmed by flow cytometry with five different antibodies, each targeting a distinct region of TTN (Figure 2A), and by wide-field fluorescence deconvolution microscopy, with photon budget readdressing increasing the detection sensitivity (Figures 2B and 2C). 3D image analysis revealed distinct intracellular distribution of the isoforms (Figure 2D), with LTTN3 confined to the cytosol, whereas LTTN1 and LTTN2 localized to both cytosol and nucleus. Flow cytometry revealed reactivity to all five TTN-specific antibodies also in B lymphocytes (Figure S2A). RNA-seq analysis confirmed *TTN* expression in these cells, covering 319 exons of the *TTN* gene (Data S2). However, unlike T lymphocytes, RNA-seq data *de novo* assembly demonstrated the reconstruction of two distinct transcripts for the *TTN* gene, clearly separated by one gap showing no sequencing reads spanning across and thus suggesting that B lymphocytes express two TTN isoforms (Data S2). These data were verified and confirmed by PCR, which showed amplification of the reconstrued transcripts, but no amplification of the regions predicted as gap (Figures S2B and S2C), confirming that human primary B lymphocytes express two TTN isoforms, each mapping to different segments of the *TTN* cDNA consensus sequence. The isoforms specific for B lymphocytes were named LTTN4 (161 exons) and LTTN5 (158 exons). As shown for *LTTN1*, RNA-seq and PCR data revealed that the *LTTN4* transcript was fused out of frame to that of *CCDC141* (Data S2). Taken together, these findings show that the *TTN* gene is constitutively expressed in human naive lymphocytes, and that T and B lymphocytes express five TTN isoforms. T lymphocytes express three TTN isoforms, encompassing a large proportion of the *TTN* gene and showing dissimilar association with DRMs and distinct intracellular distributions.

LTTN1 controls the morphogenesis of microvilli and integrin activation by chemokines

To elucidate the role of the TTN isoforms in human lymphocyte physiology, we focused on primary T lymphocytes to optimize a gene-silencing method individually targeting the isoforms. Comparative tests showed that, in contrast to LTTN2 and LTTN3 (data not shown), LTTN1 was amenable to the most effective silencing by a pool of four LTTN1-specific siRNAs, generating a uniform cell population showing a 40%–60% LTTN1 suppression within 5–6 days (Figures 3A and 3B). No reduction of LTTN2 and LTTN3 expression was observed in LTTN1-silenced cells (Figures 3C and 3D, respectively). Moreover, LTTN1 silencing did not affect cell viability (Figure 3E) or the expression of L-selectin, PSGL-1, $\beta 2$, and $\alpha 4$ integrins, or the CXCR4 chemokine receptor (Figure 3F). To verify the silencing data, we set out to estimate by MS analysis the copy number/cell of LTTN1 in control (nucleoporated with scrambled siRNAs) and LTTN1-silenced cells. By using histone protein expression as internal standard,[32,33] we estimated that approximately 25 ± 5 copies/cell of LTTN1 were expressed in control cells (n = 16), whereas 15 ± 3 copies/cell of LTTN1 were expressed in LTTN1-silenced cells (n = 16). In contrast, the copy number/cell of histone proteins remained unchanged. This was in keeping with the reduction of LTTN1 expression shown in LTTN1-silenced T lymphocytes by the cytofluorimetric analysis (Figure 3A). Notably, this quantification may provide an estimate of relative expression more than a precise calculation of protein copy number; nevertheless, it suggests that the expression of LTTN1, in term of molecules available to functional regulation, is limited in T lymphocytes.

In the context of the canonical steps of leukocyte recruitment, silencing of LTTN1 impaired the ability of T lymphocytes to establish under flow adhesive interactions at physiologic shear stress (2 dyn/cm^2) on both E-selectin and P-selectin, suggesting functional defects in L-selectin and PSGL-1 (Figure 3G). Since L-selectin and PSGL-1 expressions were unaffected in LTTN1-silenced cells, and given the well-known critical role of plasma membrane microvilli in cell capturing and rolling,[34] we hypothesized that the impairment of cell capturing under flow conditions was due to a deficiency of microvilli. This was confirmed by scanning electron microscopy (SEM), which showed that LTTN1 silencing induced the collapse of microvilli in T lymphocytes. SEM imaging showed three distinct morphologies of microvilli expression (Figure 3H), differently manifested in control versus silenced cells and likely reflecting the efficiency of LTTN1 silencing. Quantitative analysis of SEM images revealed an eight times higher percentage of the smooth phenotype in LTTN1-silenced T lymphocytes, corresponding to a cell morphology devoid of microvilli (Figure 3I). Besides, since microvilli stability is dependent on the phosphorylation state of ERM proteins,[35]

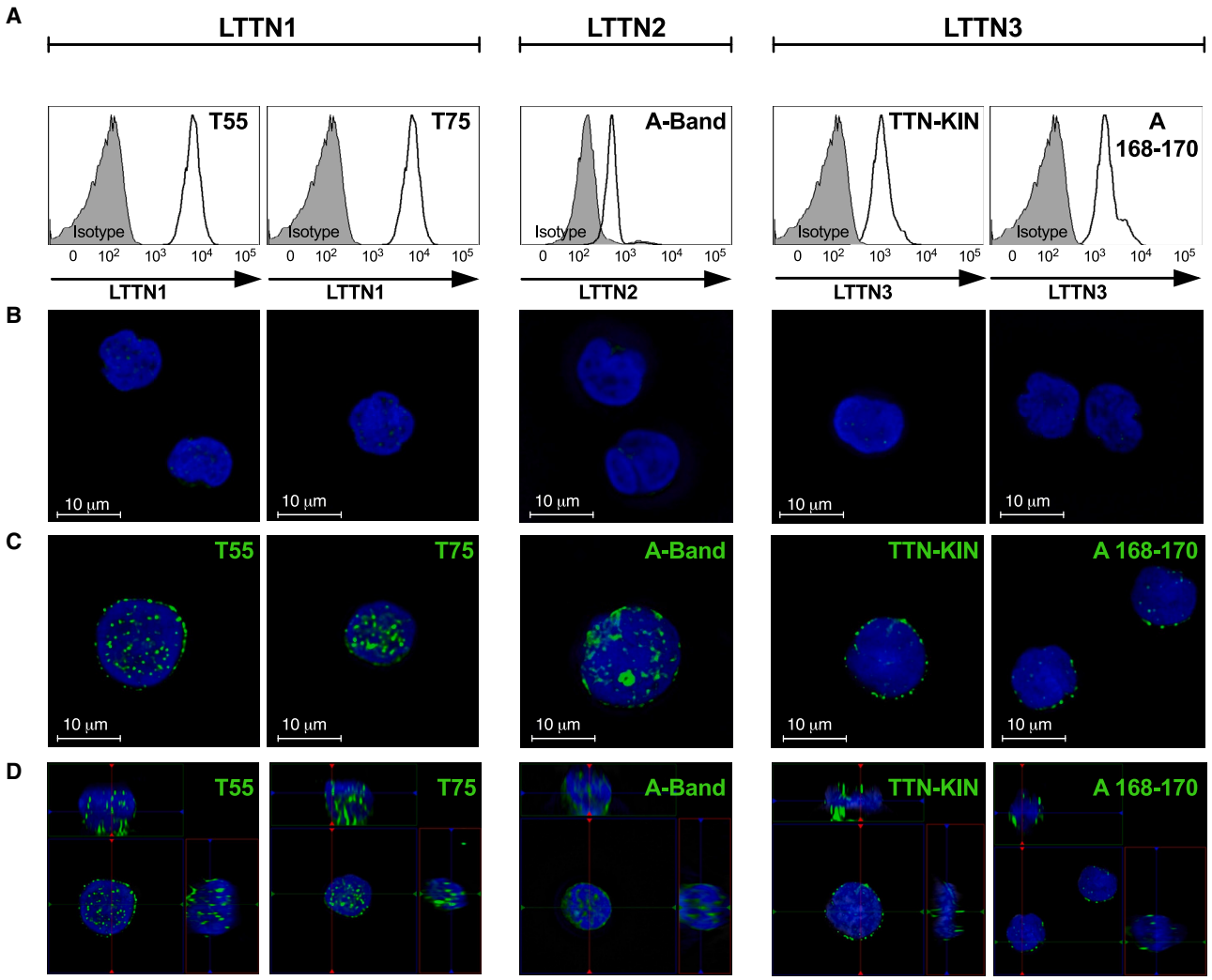

Figure 2. | Protein expression and sub-cellular localization of LTTN1, LTTN2, and LTTN3 in T lymphocytes

(A) TTN isoform expression in human T lymphocytes assessed with TTN site-specific antibodies: T55 and T75 for LTTN1, A-band Ab for LTTN2, and TTN-Kin and A168-170 for LTTN3. One representative experiment of four is shown.

(B) Fluorescence microscopy images of isotype matching control antibodies.

(C) Fluorescence microscopy images of LTTN1, LTTN2, and LTTN3 expressed in human T lymphocytes.

(D) 3D orthogonal projections showing LTTN1, LTTN2, and LTTN3 sub-cellular localization in human T lymphocytes. In (C) and (D), TTN isoforms are shown in green (labeled with the same antibodies described in A), and the nucleus is stained with DAPI (blue). Scale bars, 10 μm. One representative experiment of four is shown.

with Rac1 mediating chemokine-triggered ERM de-phosphorylation leading to microvilli collapse,[36] we investigated whether LTTN1 could control the phosphorylation state of ERM proteins. As expected, CXCL12 triggered rapid de-phosphorylation of Ezrin and Moesin, the two main ERM proteins in lymphocytes, followed by recovery within 10–30 min (data not shown). However, LTTN1 silencing did not affect chemokine-triggered de-phosphorylation of ERM proteins (Figures 4A, 4B, and 4C). Importantly, ERM protein phosphorylation was also unaffected by LTTN1 silencing in the absence of any chemokine signaling (Figures 4A, 4B, and 4C, control columns), suggesting that LTTN1 controls microvilli stability independently of the phosphorylation state of ERM proteins. These data show that LTTN1 directly controls the morphogenesis of microvilli and explains the defective capturing and rolling of LTTN1-silenced T lymphocytes under flow conditions.

Next, we evaluated the role of LTTN1 in rapid integrin activation by chemokines. LTTN1 silencing inhibited CXCL12-triggered integrin-mediated static adhesion in T lymphocytes, affecting both LFA-1-mediated adhesion to ICAM-1 and VLA-4-mediated adhesion to VCAM-1 (Figures 4D and 4E, respectively). Moreover, LTTN1 silencing reduced CXCL12-induced LFA-1 transition to heterodimeric high-affinity state (Figure 4F). Accordingly, LTTN1 silencing prevented CXCL12-triggered activation of the small GTPases RhoA by ~70% and Rac1 by ~80% (Figures 4G and 4H, respectively), with no differences

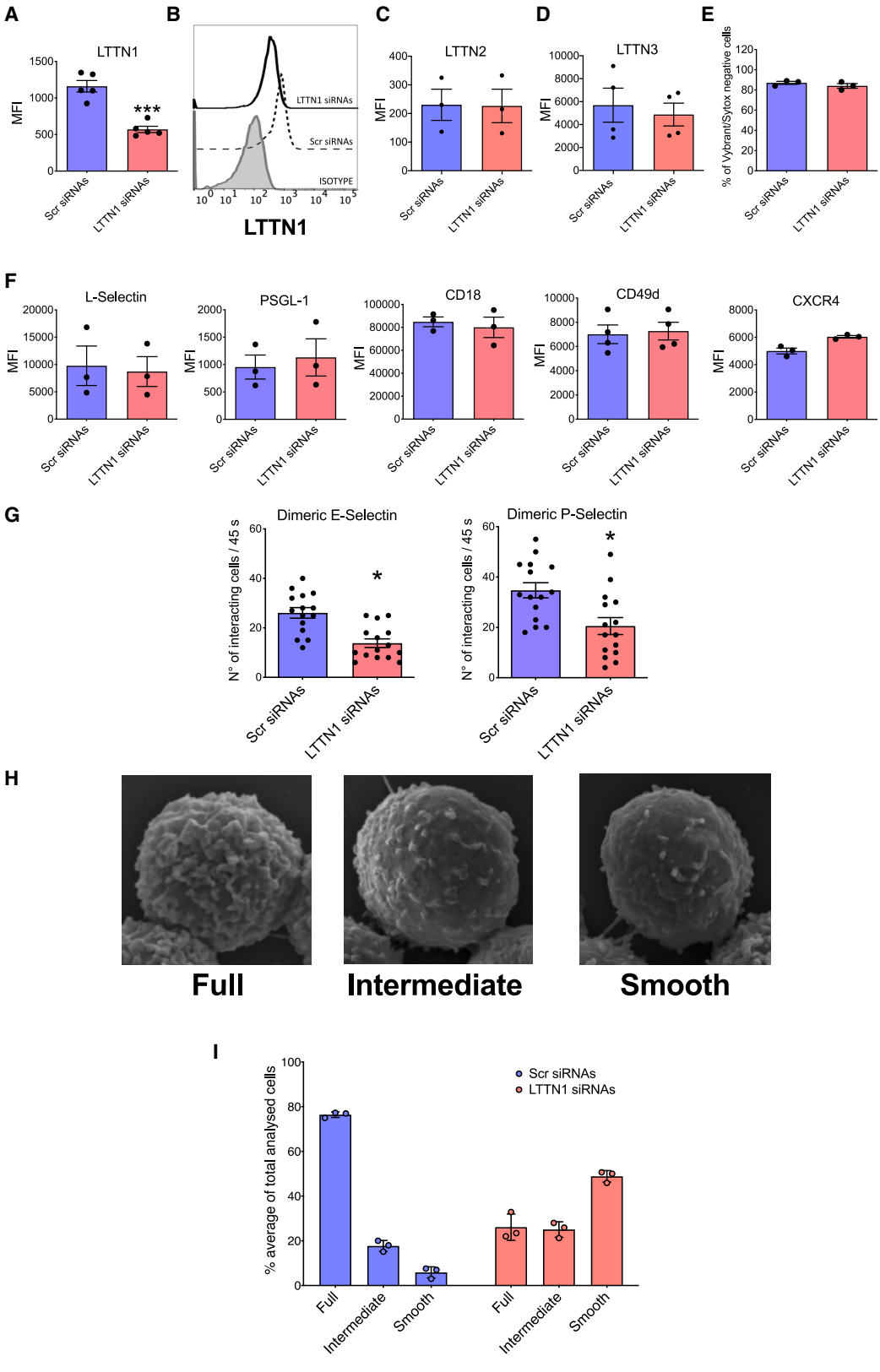

(legend on next page)

found in total RhoA and Rac1 expression (Figures 4I, 4J, 4K, and 4L). Activation of the small GTPase Rap1A was also inhibited by LTTN1 silencing, although to a lesser extent (Figures 4M and 4N). Altogether, these data show that LTTN1 controls, at the same time, the morphogenesis of microvilli and thus selectin-mediated cell capturing under flow, chemokine-triggered signal transduction, integrin activation, and mediated adhesion.

Rapid and transient downregulation of LTTN1 expression by pro-adhesive stimuli

Since TTN contributes to muscle cell passive stiffness,[23–25,37] we hypothesized that LTTN1 could likewise regulate the stiffness of T lymphocytes.[14,38–40] Therefore, LTTN1 expression should relate inversely to the acquisition of a migratory cell phenotype. Pro-adhesive molecules expressed by endothelial cells and extracellular matrix trigger in migrating leukocytes inside-out and outside-in signaling pathways leading to cell activation.[13,15,16,41] Thus, we tested whether signaling events triggered by pro-adhesive interactions could affect the expression of LTTN1. T lymphocyte activation by CXCL12 triggered LTTN1 expression to decline by ~50% in 3 min, surprisingly followed by a recovery to resting level within 30 min (Figure 5A). Notably, the very rapid but transient change in expression suggested a mechanism of LTTN1 proteolytic degradation triggered by CXCR4. Like muscle TTN,[42] LTTN1 is a possible substrate for the Ca^{2+}-dependent protease calpain (Data S3). We therefore examined whether calpain mediates the CXCR4-triggered degradation of LTTN1 in T lymphocytes. Pre-treatment with the calpain inhibitor calpeptin totally prevented LTTN1 degradation induced by CXCR4 (Figure 5B). Likewise, PSGL-1 interaction with P-selectin induced the rapid but transient downmodulation of LTTN1 expression, with complete restoration to resting level within 10–30 min (Figure 5C), which was blocked by calpeptin (Figure 5D). Finally, LFA-1 interaction with ICAM-1 induced a progressive but sustained downmodulation of LTTN1 expression, which was also prevented by calpeptin (Figure 5E). Taken together, these data suggest that the expression of LTTN1 can be rapidly downregulated during the pro-adhesive steps of T lymphocyte recruitment, and that calpain may mediate the rapid degradation of LTTN1 triggered by selectin, chemokine, and integrin signaling. Notably, calpeptin not only prevented LTTN1 degradation induced by CXCR4, PSGL-1, and LFA-1 but also induced an increase in LTTN1 expression in both resting and chemokine-activated T lymphocytes. This indicates that the expression level of LTTN1 in T lymphocytes is constitutively regulated by the balance between ongoing degradation and fast *de novo* synthesis.

LTTN1 is a negative regulator of chemokine-triggered T lymphocyte polarization and migration

We then asked whether blockade of transient LTTN1 downregulation by CXCL12 could affect T lymphocyte polarization and surface integrin redistribution triggered by chemotactic factors. Treatment with calpeptin inhibited CXCL12-triggered T lymphocyte polarization (Figures 5F, 5G, and 5H). Moreover, calpeptin inhibited LFA-1 polar redistribution induced by CXCL12 (Figure 5I). These data suggest that LTTN1 is a negative regulator of cell polarization induced by chemotactic factors. Next, we examined the role of LTTN1 in chemokine-directed chemotaxis. The actin cytoskeleton controls cell motility, so we first tested whether LTTN1 was involved in the regulation of actin polymerization. LTTN1 silencing did not affect the basal content of F-actin, or the increase in F-actin triggered by CXCL12 (Figure 5J). In Transwell migration assays, LTTN1 silencing did not inhibit migration through 3-μm pores triggered by CXCL12; on the contrary, there was a significant increase of migrated cells (Figure 5K). However, migration through 5-μm pores was neither inhibited nor potentiated by LTTN1 silencing (Figure 5L). Then, we performed chemotaxis assays across 3-μm pores with T lymphocytes treated with calpeptin to block CXCL12-induced degradation of LTTN1. We found that calpeptin treatment completely inhibited chemokine-triggered migration (Figure 5M). Notably, with respect to untreated cells (Figure 5K), calpeptin reduced migration also in LTTN1-silenced cells (Figure 5N), which, however, still presented higher migratory capability with respect to cells nucleoporated with Scr siRNAs treated with calpeptin (Figure 5N). This may not be surprising since chemotaxis is made in a population of cells showing incomplete LTTN1 silencing and that are, thus, possibly sensitive to further degradation of residual LTTN1 triggered by CXCL12. These findings show that LTTN1 does not regulate actin cytoskeleton dynamics or chemokine gradient sensing; however, a role for LTTN1 emerges when lymphocytes cross tighter gaps. Here, in keeping with the role of TTN in muscle cell stiffness,[23–25,37] LTTN1 degradation seems required to decrease the stiffness of T lymphocytes, thus facilitating their motility across small gaps.

LTTN1 controls T lymphocyte resilience to passive cell and nuclear deformation

The stability of recirculating T lymphocytes is continuously challenged by periodic passages through capillary nets, which

Figure 3. | LTTN1 controls selectin-mediated adhesion under flow by maintaining microvilli expression in T lymphocytes

(A) LTTN1 expression in human T lymphocytes nucleoporated with a pool of four scrambled (control) or four LTTN1-specific siRNAs and kept in culture for 5 days. Data are mean ± SEM (n = 6; unpaired Student's t test; ***$p < 0.001$, versus scrambled siRNAs).

(B) Representative experiment of the data shown in (A).

(C and D) LTTN2 (C) and LTTN3 (D) expression in human T lymphocytes as in (A). Data are mean ± SEM (n = 3 for C; n = 4 for D).

(E) Viability of human T lymphocytes nucleoporated as in (A) (n = 3).

(F) Expression of L-selectin, PSGL-1, CD18, CD49d, and CXCR4 in human T lymphocytes nucleoporated as in (A). Data are mean ± SEM (n = 3).

(G) Capturing and rolling under flow conditions on dimeric E-selectin and P-selectin of human T lymphocytes nucleoporated as in (A). Data are mean ± SEM (n = 3 in quintuplicate; unpaired Student's t test; *$p < 0.05$, versus scrambled siRNAs).

(H and I) Representative SEM images (H) and quantification of SEM images (I) of human T lymphocytes nucleoporated as in (A). Full, intermediate, and smooth cell morphologies were identified and plotted by analyzing multiple SEM images, including 366 cells (from 25 images) treated with scrambled siRNAs and 308 cells (from 21 images) treated with LTTN1-specific siRNAs. Percentage average data from three donors with SD are shown in (I).

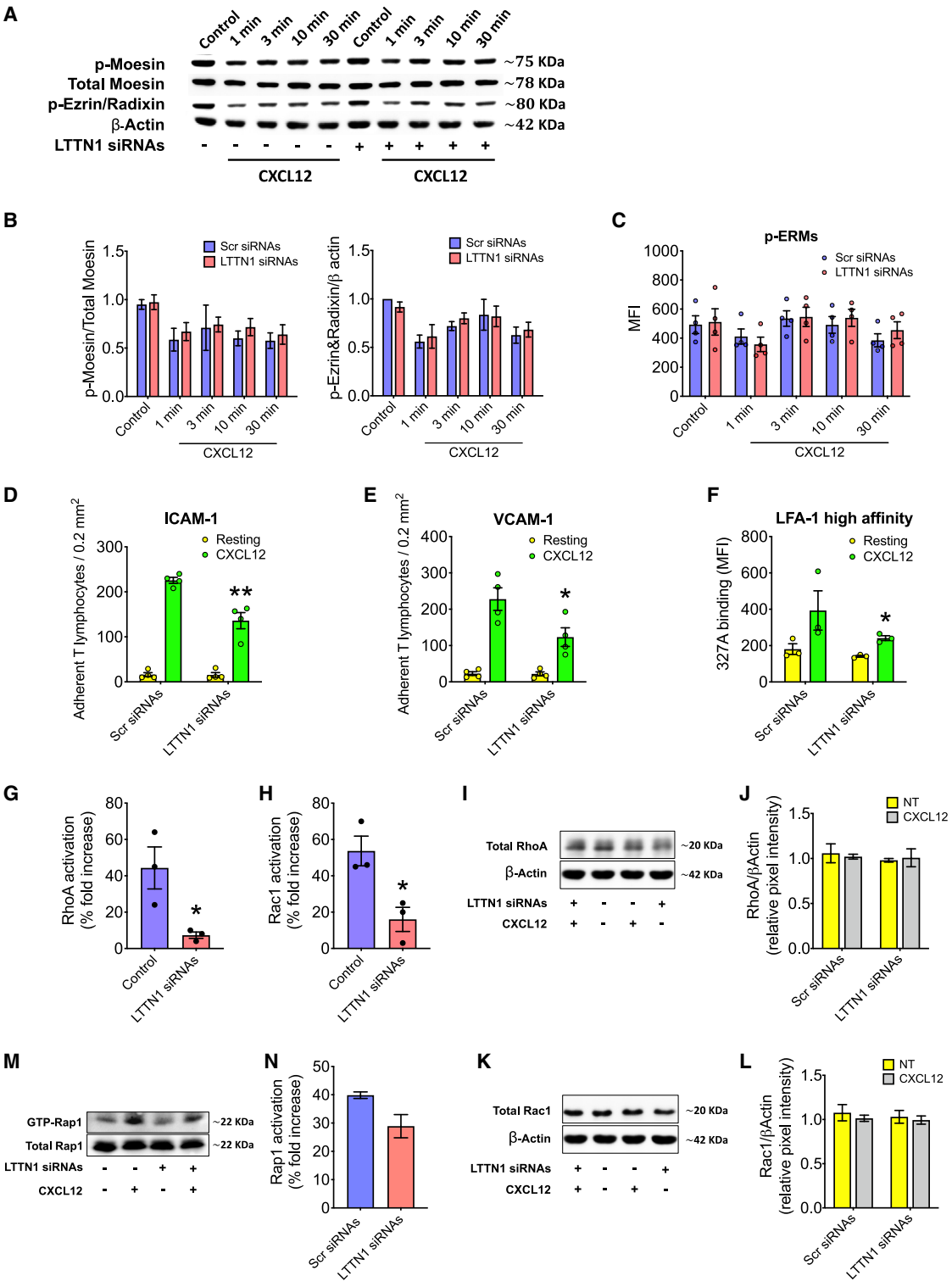

Figure 4. | LTTN1 does not control ERM protein phosphorylation but mediates chemokine-triggered signaling leading to integrin activation

(A and B) Immunoblot evaluation (A) and quantification of immunoreactive bands (B) of p-Moesin, Total Moesin, and p-Ezrin/Radixin in T lymphocytes nucleoporated with a pool of four scrambled or four LTTN1-specific siRNAs and stimulated with buffer (control) or with 200 nM CXCL12. The p-Moesin intensity was normalized to total Moesin; p-Ezrin/Radixin intensity was normalized to β-actin. Data are mean ± SEM (n = 3); one representative experiment of three is shown in (A).

(C) Flow cytometry analysis of phopsho Ezrin-Radixin-Moesin (p-ERMs) expression in cells as in (A). Data are mean ± SEM (n = 4; ANOVA followed by Tukey's test).

(legend continued on next page)

impose cell and nuclear passive deformation followed by fast shape recovery. The previous data suggest that LTTN1 may control T lymphocyte stiffness; however, in contrast with cells undergoing migration across small gaps, in circulating T lymphocytes rigidity should be preserved to confer cells resilience to passive deformation. To study mechanical stress induced by passive cell deformation under flow conditions, a microfluidic device was designed consisting of parallel microchannels with diameters narrower than the average human lymphocyte (Figures S3A and S3B). In this setting, control cells were able to cross the microfluidic constriction without damage (Figure 6A). We then tested whether the actin cytoskeleton of T lymphocytes confers resistance to passive deformation. Treatment with cytochalasin B reduced the F-actin content as expected (data not shown) but did not affect resilience to deformation (Figure 6B). In sharp contrast, stimulation with CXCL12 impaired cell resistance to passive deformation in a dose-dependent manner (Figures 6C and 6D). Notably, CXCL12 was shown to trigger a biphasic increase in $[Ca^{2+}]i$, including an influx of extracellular calcium due to the opening of calcium-operated calcium channels.[43–45] Accordingly, the presence of extracellular calcium increased the effect of CXCL12, implying a role for an intracellular calcium-dependent mechanism further potentiated by the entry of extracellular calcium (Figure 6E), thus suggesting that the effect of CXCL12 on passive cell deformation could be mediated by LTTN1 degradation triggered by calpain, whose activity was shown to be potentiated by the entry of extracellular calcium.[46] This hypothesis was tested by treating lymphocytes with calpeptin, which conferred complete resistance to the CXCL12-triggered effect and allowed the treated cells to pass through the microchannels similarly to resting cells (Figure 6F). Finally, cells stimulated with CXCL12 and left to recover for 30 min restored LTTN1 expression, as expected, along with full resilience to passive deformation (Figure 6G). Taken together, these data show that the actin cytoskeleton is not required for T lymphocyte resilience to passive deformation and that CXCL12-triggered, calpain-dependent LTTN1 degradation may be responsible for the effect of chemokine stimulation on T lymphocyte resilience to passive mechanical stress. This was confirmed by comparing LTTN1-silenced cells with those nucleoporated with scrambled siRNAs. The cells nucleoporated with scrambled siRNAs were able to cross the microchannels as easily as control cells (Figure 6H); in contrast, LTTN1 silencing strongly impaired the resilience of T lymphocytes to deformation (Figure 6I). The silenced cells were unable to cross the microfluidic channels and were destroyed immediately after crossing the initial microchannel constriction. Together, these data suggest that LTTN1 controls the deformability of T lymphocytes, providing the necessary stiffness to counteract the passive deformation occurring in microchannels (Figures 6J and 6K).

To further support these findings, we tested T lymphocytes for resistance to hypo-osmotic shock, a test previously adopted to study cell deformability.[47] In cells nucleoporated with scrambled siRNAs, osmotic shock induced time-dependent swelling accompanied by cell damage, whereas no such effects were seen in control cells maintained in an isosmolar environment, as expected. In contrast, in LTTN1-silenced cells, osmotic shock triggered swelling and cell damage more effectively, with an 80% drop in the number of undamaged cells (Figures 7A, 7B, and 7C). This protocol did not cause nuclear disruption. These data show that LTTN1 controls T lymphocyte resistance to osmotic shock, further supporting its role in maintaining cell body resistance to passive mechanical stress.

LTTN1 preserves the cellular integrity of T lymphocytes in the microcirculation

The previous data suggest that LTTN1 deficiency could affect the survival of T lymphocytes in the microcirculation, where mechanical stress due to passive deformation induced by crossing capillary nets continuously occurs. To test this hypothesis, cells nucleoporated with Scr siRNAs (control) or with LTTN1-specific siRNAs were injected intravenously in mice, and after 30 min the relative abundance of controls and silenced cells in the lung vessels was determined. The cells were alternatively labeled with different fluorochromes to reveal possible non-specific effects. Fluorescence microscopy showed a clear imbalance between control cells and LTTN1-silenced cells in the lung vasculature, with a consistent loss of silenced cells (Figures S4 and S5). Indeed, quantification by image analysis of multiple serial tissue sections taken from different pulmonary lobes showed a consistent decline in the proportion of silenced cells, ranging from −38% to −76% (Figures 7D and 7E). Pooled image quantification data from all lobes and lungs analyzed showed an overall 54% reduction in the number of LTTN1-silenced T cells (Figure 7F). In agreement with these data, quantification by flow cytometry of the relative number of fluorescently labeled cells, both in blood samples and in lung lysates, showed a significative reduction of LTTN1-silenced T cells with respect to control cells (Figures 7G and 7H).

Last, to directly assess in real time the resilience of LTTN1-silenced T lymphocytes to passive deformation occurring in the microcirculation, an established intravital microcopy setting was applied to directly visualize the microcirculation within muscle vasculature, where an extensive texture of parallel capillaries is present.[44–46] Fluorescently labeled T lymphocytes, either nucleoporated with Scr siRNAs or with LTTN1-specific siRNAs,

(D and E) Static adhesion assay on ICAM-1 (D) or VCAM-1 (E) of human T lymphocytes nucleoporated as in Figure 3A, stimulated with buffer (control) or with 200 nM CXCL12. Data are mean ± SEM (n = 4 in triplicate; unpaired Student's t test; $^{**}p < 0.01$, $^{*}p < 0.05$, versus scrambled siRNAs).
(F) LFA-1 high-affinity measurement of cells as in (D). Data are mean ± SEM (n = 3; unpaired Student's t test; $^{*}p < 0.05$, versus scrambled siRNAs).
(G and H) Small G-protein linked immunosorbent assay (G-LISA) assay detecting RhoA (G) and Rac1 (H) activation in human T lymphocytes nucleoporated as in (D). Fold increase of RhoA or Rac1 activation was normalized to intensity in untreated controls. Data are mean ± SEM (n = 3; unpaired Student's t test; $^{*}p < 0.05$, versus scrambled siRNAs).
(I–L) immunoblot evaluation and quantification of immunoreactive bands of RhoA (I and J) and Rac1 (K and L) in cells as in (D). RhoA and Rap1 intensity was normalized to β-actin. Data are means ± SEM (n = 3); one representative experiment of three is shown in (I) and (K).
(M and N) Immunoblot evaluation (M) and quantification (N) of immunoreactive bands of Rap1A activation in human T lymphocytes nucleoporated as in (D). GTP-Rap1A intensity was normalized to total Rap1A intensity. One representative experiment of three is shown.

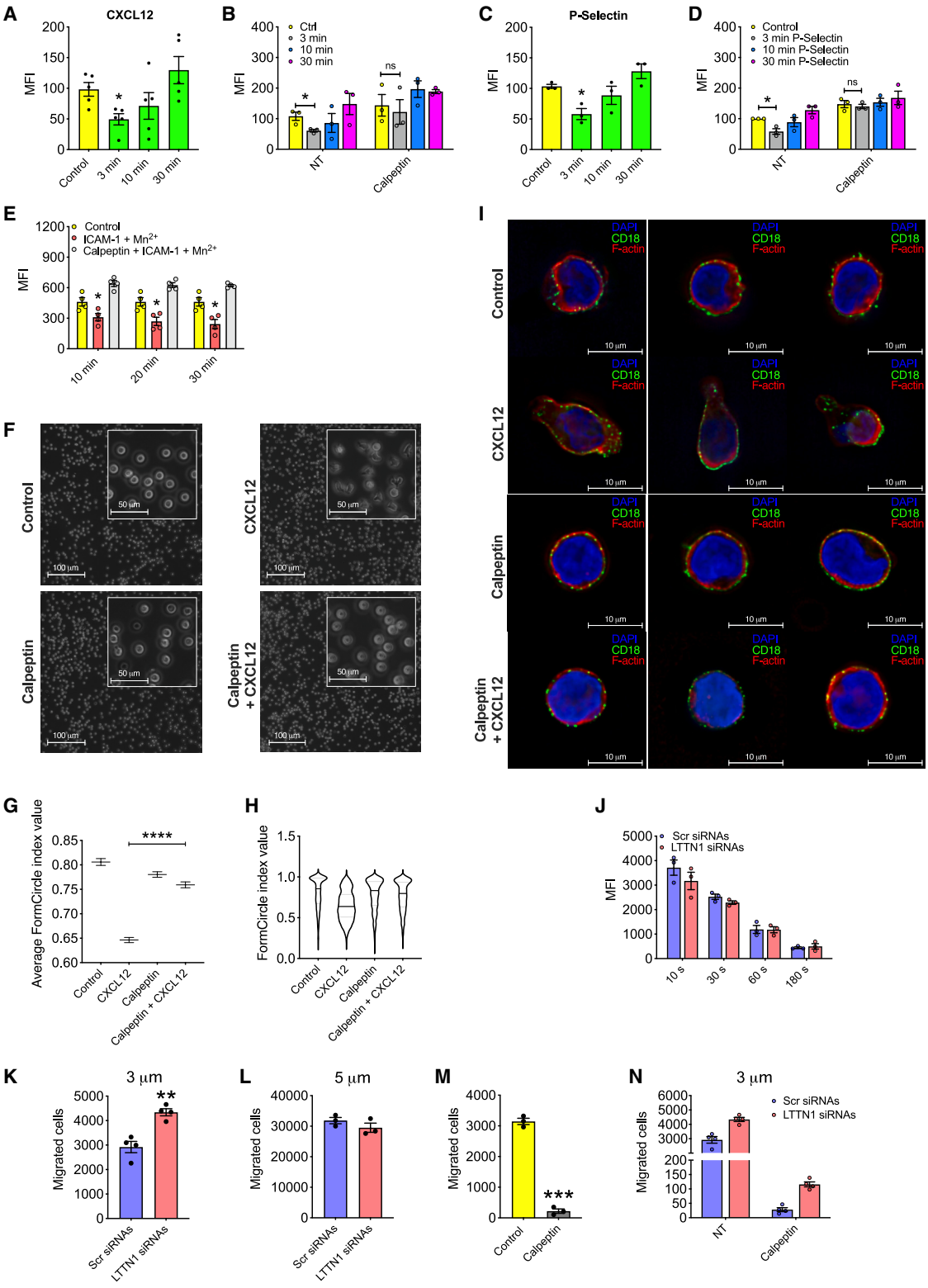

Figure 5. Control of LTTN1 expression by pro-adhesive stimuli and role in cell polarization

(A) LTTN1 expression in human T lymphocytes unstimulated (control) or stimulated with 200 nM CXCL12 for the indicated times (n = 5).

(B) LTTN1 expression in human T lymphocytes pre-treated with DMSO (NT) or 150 µg/mL calpeptin for 30 min at 37°C and stimulated as in (A) (n = 3).

(C) LTTN1 expression in human T lymphocytes unstimulated (control) or stimulated with 10 µg/mL dimeric P-selectin for the indicated times (n = 3).

(legend continued on next page)

were injected directly in the mouse right carotid, thus allowing immediate arrival of the cells into the pectoral muscle vasculature, avoiding previous passage through other organs.[48–50] This experimental setting showed that cells nucleoporated with Scr siRNAs progressively accumulate in the pectoral muscle microcirculation at early time points (5 min) and remain entrapped for prolonged time (20 min) (Figure S6). In contrast, LTTN1-silenced cells accumulated in the microcirculation similarly to control cells at early time points (5 min) but progressively disappeared at late time points (20 min) (Figure S6). This was not exclusively due to cell disengagement from the microcirculation to come back to the blood flow; indeed, frame-by-frame video analysis showed that, compared with control cells, an almost three times higher percentage of LTTN1-silenced cells manifested, with respect to the blood flow direction, a progressive intravascular rear leakage of cell fluorescent content, a morphology indicating cell damage under flow (Figures 7I and 7J; Video S1). Altogether, these data are in keeping with the previous *in vitro* and *in vivo* experiments and indicate that LTTN1 provides circulating T lymphocytes the resilience to mechanical stress induced by passive deformation in the microcirculation.

DISCUSSION

In this study we provide evidence that human lymphocytes express five novel TTN isoforms and that at least one, LTTN1, controls, at the same time, different steps of lymphocyte recruitment such as cell capturing under flow, signaling mechanisms leading to integrin activation by chemokines, and cell deformability. T lymphocytes express three TTN isoforms (LTTN1, LTTN2, and LTTN3), whereas two further isoforms (LTTN4 and LTTN5) are expressed in B lymphocytes. High-sensitivity fluorescence microscopy showed that LTTN1 and LTTN2 occupy both the cytosolic and nuclear compartments, whereas LTTN3 is confined to the cytosol. Moreover, MS analysis detected LTTN1 and LTTN2, but not LTTN3, in T lymphocyte DRMs. Given that DRMs are nanoscale structures, the much larger LTTN1 and LTTN2 isoforms, with an estimated size of about 300 and 620 nm respectively, are unlikely to be confined within them. It is therefore conceivable that LTTN1 and LTTN2 extend from DRMs into the cell interior. Notably, LTTN1 and LTTN2 show protein domain arrangements like canonical TTN, suggesting interactome properties comparable with those of muscle TTN. Thus, we hypothesized that, in T lymphocytes, DRMs can be anchors for LTTN1 and LTTN2, and that these isoforms extend from DRMs into the cell, generating an intracellular mechano-scaffolding skeleton, perhaps by means of homophilic and/or heterophilic multimeric interactions,[25,51] that control the signaling and mechanical properties of human T lymphocytes.

A focus of our study was to test whether LTTN1 could regulate cell stiffness and deformability in T lymphocytes. Four distinct findings supported this hypothesis. First, LTTN1 is rapidly degraded in a calpeptin-sensitive manner by either chemokine or integrin signaling. This establishes an inverse correlation between LTTN1 expression and the activity of pro-adhesive mediators regulating cell polarization, spreading, and motility, which are characterized by increased cell plasticity.[17,52] Second, LTTN1 appears to be a negative regulator of cell plasticity because cells that cannot degrade LTTN1 are unable to polarize and to squeeze through, and overstep, small gaps. Third, LTTN1 silencing does not prevent migration, but it does facilitate it, which requires the reduction in cell stiffness to favor deformability.[17] Finally, in LTTN1-silenced T lymphocytes, the resilience to passive cell deformation is compromised, with both cell body and nucleus destroyed by passive mechanical stress *in vitro*. Furthermore, LTTN1 deficiency reduces the resilience of T lymphocytes to osmotic shock and affects their cellular integrity in the microcirculation. Taken together, these data support a dual role for LTTN1 in T lymphocyte trafficking: accordingly, LTTN1 seems necessary to provide resting T lymphocytes with sufficient rigidity to tolerate the mechanical stress induced by passive deformation occurring in the microcirculation, but its degradation appears indispensable for the migration. Thus, LTTN1 seems to regulate both passive and active cell deformability.

LTTN1 also controls the canonical steps of T lymphocyte adhesion under flow conditions. LTTN1 silencing impaired selectin-mediated capturing and rolling, and this was in keeping with the collapse of surface microvilli. Interestingly, LTTN1 silencing did not affect chemokine-triggered de-phosphorylation of ERM proteins. This could possibly contrast with the reported role of Rac1 in the de-phosphorylation of ERM proteins induced by chemokines. However, since LTTN1 silencing did not entirely

(D) LTTN1 expression in T lymphocytes pre-treated as in (B) and stimulated as in (C) (n = 3).
(E) LTTN1 expression in human T lymphocytes untreated (control) or treated with 1 mM Mn^{2+} and exposed to immobilized ICAM-1 or pre-treated as in (B) and then treated with 1 mM Mn^{2+} and exposed to immobilized ICAM-1. LTTN1 expression was evaluated at the indicated times (n = 3). In (A)–(E), data are mean ± SEM; ANOVA followed by Dunnett's *post hoc* test; *p < 0.05, versus control.
(F) Polarization of resting T lymphocytes (control), T lymphocytes stimulated with 0.2 μM CXCL12, T lymphocytes pre-treated with 150 μg/mL calpeptin, and T lymphocytes pre-treated with 150 μg/mL calpeptin and stimulated with 0.2 μM CXCL12; image square frames show 40× magnification. Scale bars, 100 μm (20×) and 50 μm (40×).
(G and H) Average FormCircle (G) and FormCircle index value distribution (H) analysis of cells treated as in (F). Data are mean ± SD (control n = 782, CXCL12 n = 1,123, calpeptin n = 962, calpeptin + CXCL12 n = 1105; unpaired Student's t test; ****p < 0.0001).
(I) Immunofluorescence evaluation of CD18 (green) expression in T lymphocytes treated as in (F). F-actin and nuclei are shown in red (SiR-actin_CY5) and blue (DAPI), respectively; three representative cells for every condition are shown; one representative experiment of three. Scale bars, 10 μm.
(J) F-actin polymerization in human T lymphocytes nucleoporated as in Figure 3A. Cells were stimulated with 200 nM CXCL12 for the indicated times. Data are mean ± SEM (n = 3).
(K and L) Migration assays through 3 μm (K) or 5 μm (L) Transwells of human T lymphocytes nucleoporated as in Figure 3A (in K, n = 4; in L, n = 3).
(M) Migration assay as in (K) in human T lymphocytes untreated (control) and treated with 150 μg/mL calpeptin for 30 min at 37°C (n = 3).
(N) Migration assay as in (K) of human T lymphocytes untreated (NT) or pre-treated as in (M) (n = 4). In (K)–(M), data are mean ± SEM (unpaired Student's t test; **p < 0.01, ***p < 0.001, versus scrambled siRNAs). See also Data S3.

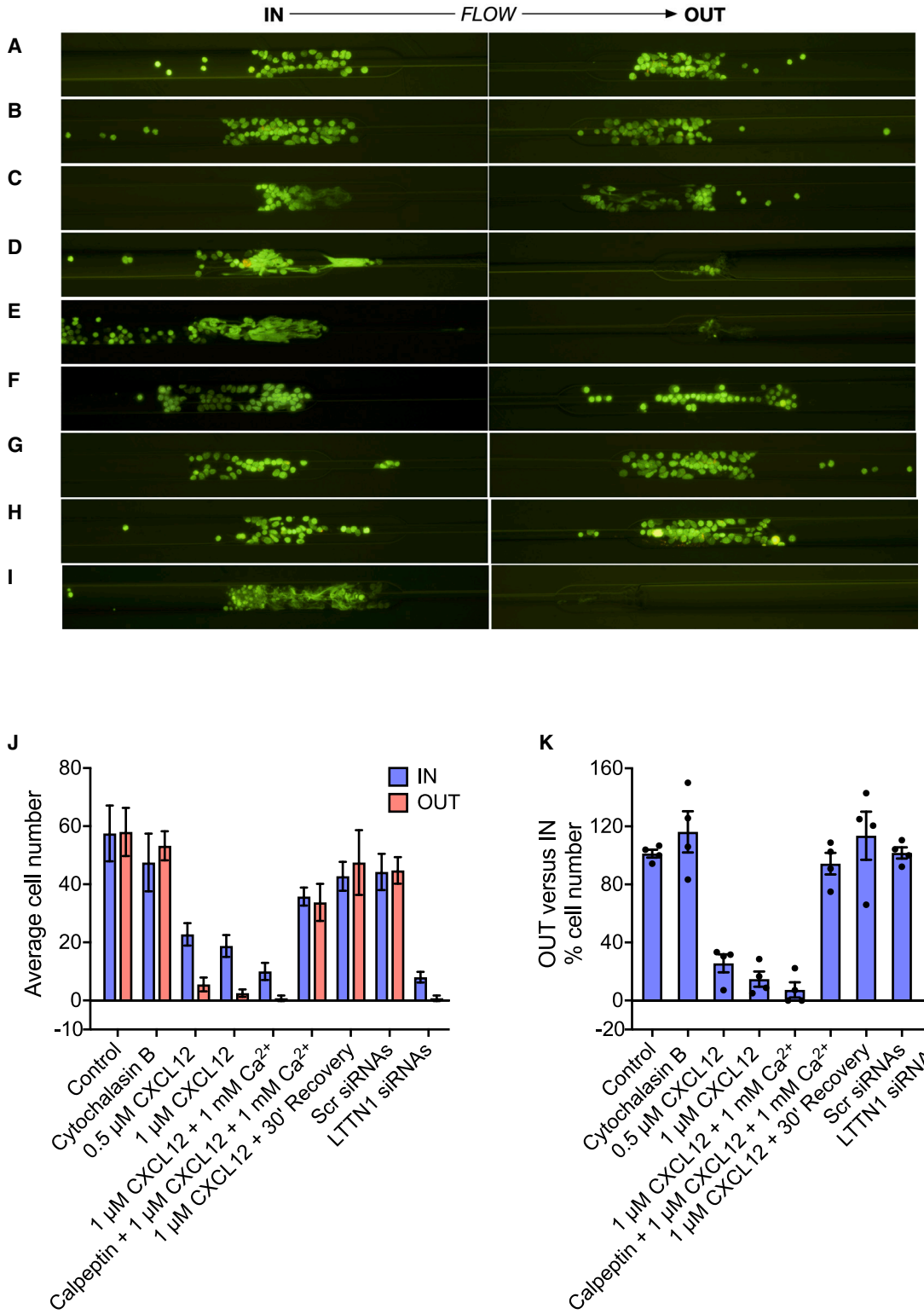

Figure 6. | LTTN1 controls the resilience of T lymphocytes to passive cell deformation in microfluidic setting

(A–I) Fluorescence microscopy images showing individual channels in the microfluidic device designed to study passive cell deformability under flow conditions. Cells were labeled with AO. (A) Control human T lymphocytes. (B) Human T lymphocytes treated with 5 μg/mL cytochalasin B for 30 min at 37°C. (C) Human T lymphocytes stimulated with 0.5 μM CXCL12 for 3 min at 37°C. (D) Human T lymphocytes stimulated with 1 μM CXCL12 for 3 min at 37°C. (E) Human T

(legend continued on next page)

abolish Rac1 activation, it is possible that the residual Rac1 activity is sufficient to mediate ERM protein de-phosphorylation induced by chemokines in LTTN1-silenced cells. Importantly, in the absence of any chemokine signaling, constitutive ERM protein phosphorylation was completely unaffected by LTTN1 silencing, suggesting that LTTN1 may control microvilli expression independently of the phosphorylation state of ERM proteins. Overall, the data suggest that LTTN1 and ERM proteins concurrently control microvilli structure and function and that chemokines may lead to microvilli collapse by triggering, at the same time, Rac1-mediated ERM protein de-phosphorylation and calpain-mediated LTTN1 degradation. In muscle cells, TTN interacts with actin and actin-binding proteins.[53,54] Accordingly, LTTN1 could generate an intracellular meshwork beneath the plasma membrane, anchoring actin-binding proteins, or the actin cytoskeleton backbone, within the microvilli. Upon LTTN1 degradation, the actin backbone could lose support, causing the microvilli to collapse. Notably, microvilli are now recognized as platforms of receptor aggregation and signal transduction.[55] Thus, the critical role of LTTN1 in the morphogenesis of microvilli may provide insights on their homeostasis and function, beyond their classical role in leukocyte capturing and rolling. Interestingly, as with chemokines and integrins, PSGL-1 triggers LTTN1 degradation. Thus, PSGL-1 relies on LTTN1-controlled microvilli integrity to mediate cell capturing but, at the same time, appears capable of triggering LTTN1 degradation, possibly leading to the collapse of microvilli. This apparent paradox could hypothetically represent a homeostatic mechanism. Indeed, by successively mediating capturing/rolling and LTTN1 degradation, PSGL-1 could potentially establish a temporal threshold to the duration of rolling.

LTTN1 likewise regulates rapid LFA-1 and VLA-4 integrin activation by chemokines. This was in keeping with the data showing that LTTN1 silencing prevents RhoA, Rac1, and Rap1A activation by CXCL12. Because LTTN1 lacks kinase activity, which in T lymphocytes is possibly restricted to the LTTN3 isoform, it is likely that LTTN1 regulates integrin activation via docking-scaffolding mechanisms. We have previously shown that at least four rho guanine nucleotide exchange factor (GEF) domains mediate the CXCL12-triggered activation of rho GTPases,[56] concurrently regulated by JAK and BTK protein tyrosine kinases.[57,58] LTTN1 could, therefore, regulate the activity of these intermediates.

Collectively, the data could suggest an LTTN1-centric model of T lymphocyte trafficking. In this model, circulating T lymphocytes rely on LTTN1 to maintain the stiffness to cope with passive deformation in the microcirculation. LTTN1 may ensure the survival of circulating cells until a permissive endothelium is engaged. Here, LTTN1 is critical to maintain microvilli, allowing the presentation of the molecules required for cell capturing and rolling. However, a checkpoint could occur during rolling, due to PSGL1-triggered degradation of LTTN1. Then, the arrested cells need to remove intracellular mechanical constraints to actomyosin-based contractile forces to generate pseudopods. In keeping with the role of TTN in muscle cell stiffness and with our data, LTTN1 degradation is essential at this stage to reduce stiffness, increasing cell plasticity. During chemotaxis LTTN1 expression is kept low by concurrent inside-out and outside-in signaling generated by chemokines and integrins. Eventually, T lymphocytes may come back to the circulation, where stiffness must be restored to ensure resilience to passive deformation. The very rapid expression turnover of LTTN1 may facilitate this process. Notably, considering the huge size of LTTN1, its very fast resynthesis after degradation could be surprising. However, recent data regarding the capability of naive T lymphocytes to control very rapid and consistent protein turnover, mainly with autophagic pathway, may support this finding. Indeed, it was recently shown that naive T lymphocytes, far from being metabolically quiescent cells, do possess a fast dynamic program of very rapid protein turnover, leading to fast and consistent protein synthesis, with about 60,000 proteins/min synthesized.[59,60] This protein synthesis does not lead to progressive protein content increase, suggesting an ongoing equilibrium between incessant protein replenishment and loss. Moreover, naive T lymphocytes rely on autophagy of key proteins to sustain protein turnover critical to survival,[61] with calpain involved in autophagy regulation.[62,63] Thus, the data showing that calpeptin treatment alone leads to rapid increase of LTTN1 expression in resting T lymphocytes (see Figure 5) suggest that LTTN1 content is possibly regulated according to this balanced protein degradation/synthesis program, constitutively at work in naive T cells. Therefore, the trafficking of T lymphocytes could be subjected to tight spatiotemporal regulation by the fast expression turnover of LTTN1.

Several questions arise from our study, including the mechanism by which LTTN1 is anchored to DRMs, the regulation of membrane tubulation controlling the morphogenesis of microvilli, the regulation of chemokine-triggered integrin activation, and the possible cooperation of LTTN1 with molecules proposed to maintain cell and nuclear stiffness and shape, such as vimentin,[64,65] the linker of nucleoskeleton and cytoskeleton (LINC) complex,[17,66] and lamins.[67,68] It is also important to evaluate the role of LTTN1 in T cell receptor function, which is almost exclusively localized on microvilli.[69] Moreover, considering the proposed role of TTN in chromosome structure and segregation,[70–73] it will be interesting to determine whether the detected nuclear localization of LTTN1 may suggest a role in the regulation of T lymphocyte gene expression or maturation. Interestingly, a functional nuclear localization sequence (NLS), 200-PAKKTKT-206, located in a low-complexity, titin-specific region between Z2 and Z repeats, was found in previous studies.[74] We checked the presence of this NLS sequence in the LTTN isoforms and

lymphocytes stimulated with 1 μM CXCL12 for 3 min in buffer containing 1 mM Ca^{2+}. (F) Human T lymphocytes treated with 150 μg/mL calpeptin for 30 min at 37°C and then stimulated with 1 μM CXCL12 for 3 min in buffer containing 1 mM Ca^{2+}. (G) Human T lymphocytes stimulated with 1 μM CXCL12 for 3 min at 37°C and left to recover for 30 min 37°C. (H) Human T lymphocytes nucleoporated with four scrambled siRNAs and cultured for 5 days. (I) Human T lymphocytes nucleoporated with four LTTN1-specific siRNAs and cultured for 5 days. (A–I) One representative microchannel from four experiments is shown.
(J) Quantification of the average cell number observed in the "IN" and "OUT" side of the microfluidic device (see also Figures S3A and S3B).
(K) Quantification of the percentage cell number engaging the "IN" and "OUT" side of the microfluidic device (in J and K, n = 4).

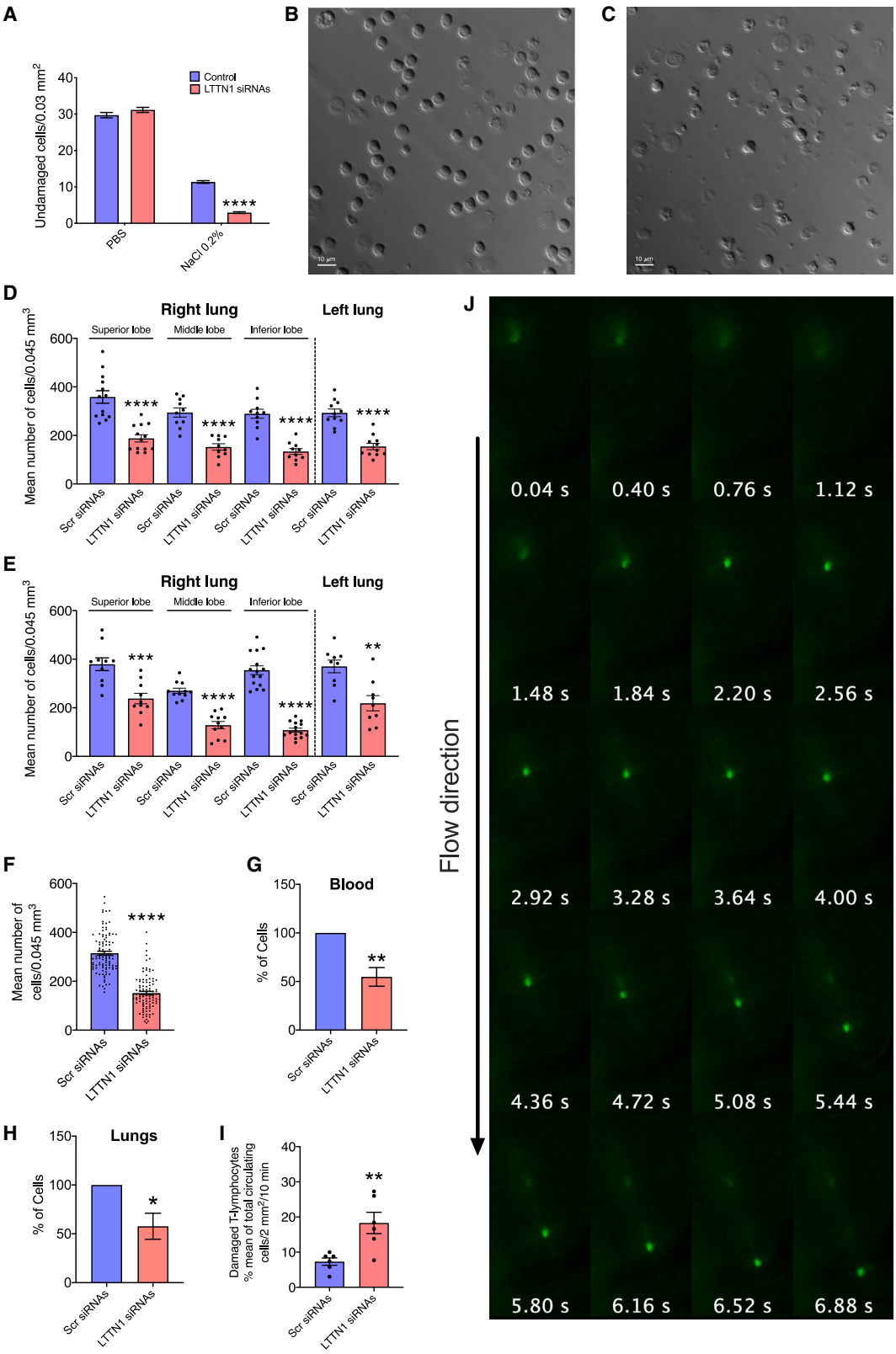

(legend on next page)

found it in LTTN1 (amino acid 214-PAKKTKT-222). This could possibly explain the nuclear localization of at least LTTN1. Finally, the functional roles of the other four isoforms need to be defined.

TTN is a major determinant of cardiomyocyte stiffness and contributor to cardiac strain sensing. Due to the enormous size, complexity, and malleability of the titin molecule, TTN is also vulnerable to dysregulation, as observed in various cardiac disorders. Accordingly, the *TTN* gene is structured to accommodate extensive splicing,[75] and many genetic variants have been described.[76] In this context, it could be possible that changes in structure and/or expression of the leukocyte TTN isoforms might play a role in pathologies involving immune cells. For instance, certain diseases are characterized by the alteration of leukocyte rigidity leading to diffuse intravascular leukostasis, for example in pulmonary distress syndrome[77,78] and acute leukemia.[79,80] The molecular basis of leukostasis is poorly defined, and the role of LTTN1 in the stiffness and survival of circulating T lymphocytes could provide a further line of investigation. Therefore, it will be of great interest to investigate whether variants of the identified lymphocyte TTN isoforms may occur in pathology.

Limitations of the study

The role of LTTN1 in controlling T lymphocyte stiffness was not complemented by atomic force microscopy (AFM) quantitative analysis. Moreover, the role of LTTN1 in microvilli morphogenesis was not completely clarified; particularly, it is necessary to understand how LTTN1 may stabilize microvilli structure independently of the phosphorylation state of ERM proteins. Furthermore, it is unclear how LTTN1 mediates activation of rho and rap small GTPases. Last, we showed that, in both the silenced cells and those stimulated with CXCL12, the deformation induced by microchannels disrupted not only the cell body but also the nucleus, as shown by the massive leakage of stained nucleic acids into the fluidic device. This may suggest that LTTN1 could be also critical to preserving nuclear integrity. However, it is also possible that, in LTTN1-silenced cells, the nucleus, upon cell disruption and, thus, outside the context of the whole cell, simply becomes more sensitive to the shear force of the device, thus undergoing disruption independently of a role for LTTN1. This point needs to be further investigated with dedicated experimental settings.

STAR★METHODS

Detailed methods are provided in the online version of this paper and include the following:

- KEY RESOURCES TABLE
- RESOURCE AVAILABILITY
  - Lead contact
  - Materials availability
  - Data and code availability
- EXPERIMENTAL MODELS AND SUBJECT DETAILS
  - Mice
  - Human
- METHOD DETAILS
  - Isolation of human primary cells
  - Purification of DRM fraction
  - MUD-PIT analysis
  - Analysis of DRM interactome
  - RNA extraction
  - RNA sequencing and RNA-seq data processing
  - Analysis of LTTN isoforms expression by PCR
  - LTTN isoforms expression by flow cytometry
  - Sub-cellular localization of LTTN isoforms by IF
  - LTTN1 silencing by small interfering RNA
  - Cell viability
  - Pro-adhesive molecules expression by flow cytometry
  - Cp-ERMs and moesin expression
  - Under-flow adhesion assay
  - Analysis of surface microvilli expression by SEM
  - Static adhesion assay
  - Measurement of LFA-1 high-affinity state
  - RhoA and Rac1 activation
  - Western blot of total RhoA and Rac1 expression
  - Rap1 activation
  - F-actin staining
  - Cell polarization assay
  - Chemotaxis assay
  - Deformability assay in microfluidic channels

Figure 7. | LTTN1 controls the resilience of T lymphocytes to osmotic shock and to passive cell deformation in muscle microcirculation

(A) Quantification of resilience to hypo-osmotic shock in human T lymphocytes nucleoporated as Figure 3A; human T lymphocytes were suspended in PBS or 0.2% NaCl and incubated for 30 min at 37°C. One representative experiment of four is shown.

(B and C) Differential interference contrast (DIC) images of control (B) or LTTN1-silenced human T lymphocytes (C) in 0.2% NaCl after 30 min. Representative images of 50. Scale bars, 10 μm.

(D–F) Permanence of human T lymphocytes in mouse blood circulation deduced from the mean number of cells per volume of pulmonary tissue. Dots represent individual analyzed images. (D) Control cells nucleoporated with Scr siRNAs (CMTMR) and LTTN1-silenced cells (CMTPX). (E) Control cells nucleoporated with Scr siRNAs (CMTPX) and LTTN1-silenced cells (CMTMR). One representative experiment of three; see also Figures S4 and S5. (F) Aggregated and averaged data from (D) and (E). Error bars indicate SD (A) or SEM (D–F). Unpaired Student's t test; ***$p < 0.001$, versus scrambled siRNAs.

(G and H) Permanence of human T lymphocytes nucleoporated as in Figure 3A in mouse blood (G) and in lung lysates (H); quantification was after 30 min from the injection; control (Scr siRNAs) and LTTN1-silenced cells were alternatively labeled with CMAC and CMFDA and data were merged in the same plot. Data were normalized to scrambled siRNAs. Unpaired Student's t test, *$p < 0.05$ ($n = 5$).

(I) Quantification of cells manifesting a progressive intravascular rear release of cell AO-labeled content in control (Scr siRNAs) and LTTN1-silenced (LTTN1 siRNAs) human T lymphocytes. Data are percentage mean in six fields from three experiments ±SEM (unpaired Student's t test; **$p < 0.01$ versus Scr siRNAs).

(J) Fluorescence microscopy images of AO-labeled LTTN1-silenced human T lymphocyte entrapped in the microcirculation and manifesting a progressive intravascular rear release of cell AO-labeled content. Shown is a temporal sequence of about 7 s. One representative cell from three experiments is shown; see also Figure S6 and Table S4.

- Hypoosmotic shock
- Permanence of T lymphocytes in mouse circulation
- Flow cytometry on mouse blood and lungs homogenates
- Intravital microscopy in muscle microcirculation

- QUANTIFICATION AND STATISTICAL ANALYSIS

SUPPLEMENTAL INFORMATION

Supplemental information can be found online at https://doi.org/10.1016/j.celrep.2023.112516.

ACKNOWLEDGMENTS

This work was supported by Italian Association for Cancer Research (AIRC, IG-16797), Fondazione per la Ricerca sulla Fibrosi Cistica (FFC), grants #13/2019 and #7/2021, Fondo Unico Ricerca (FUR) and JointProject 2017 University of Verona, the European Research Council (ERC) Advanced Grant #695714 IMMUNOALZHEIMER (G.C.) and NEXTGENERATIONEU - the Italian Ministry of University and Research, National Recovery and Resilience Plan (NRRP), project MNESYS (PE0000006) (G.C.). We thank Dr. Richard M. Twyman (Twyman Research Management, https://www.twymanrm.com) for revision of the manuscript.

AUTHOR CONTRIBUTIONS

Conceptualization, C.L., L.T., C.G., and P.M.; methodology, L.T., C.G., P.M., A.S., W.A.L., G.C., M.D., and C.L.; investigation, L.T., C.G., B.D.U., A.M., W.A.L., M.R., B.I., B.R., P.B., G.A., N.L., A.U., D.D., L.B., A.D.P., S.M., and C.L.; visualization, L.T., C.L., D.D.D., M.R., and B.I.; funding acquisition, C.L. and G.C.; supervision, C.L.; writing – original draft, C.L., L.T., and B.D.U.

DECLARATION OF INTERESTS

The authors declare no competing interests.

INCLUSION AND DIVERSITY

We support inclusive, diverse, and equitable conduct of research.

Received: November 21, 2022
Revised: March 24, 2023
Accepted: May 1, 2023

REFERENCES

1. Chaplin, D.D. (2010). Overview of the immune response. J. Allergy Clin. Immunol. *125*, S3–S23. https://doi.org/10.1016/j.jaci.2009.12.980.
2. Zhu, C., Bao, G., and Wang, N. (2000). Cell mechanics: mechanical response, cell adhesion, and molecular deformation. Annu. Rev. Biomed. Eng. *2*, 189–226. https://doi.org/10.1146/annurev.bioeng.2.1.189.
3. Chen, C.S. (2008). Mechanotransduction - a field pulling together? J. Cell Sci. *121*, 3285–3292. https://doi.org/10.1242/jcs.023507.
4. Tarbell, J.M., Simon, S.I., and Curry, F.R.E. (2014). Mechanosensing at the vascular interface. Annu. Rev. Biomed. Eng. *16*, 505–532. https://doi.org/10.1146/annurev-bioeng-071813-104908.
5. Elosegui-Artola, A., Oria, R., Chen, Y., Kosmalska, A., Pérez-González, C., Castro, N., Zhu, C., Trepat, X., and Roca-Cusachs, P. (2016). Mechanical regulation of a molecular clutch defines force transmission and transduction in response to matrix rigidity. Nat. Cell Biol. *18*, 540–548. https://doi.org/10.1038/ncb3336.
6. Jansen, K.A., Atherton, P., and Ballestrem, C. (2017). Mechanotransduction at the cell-matrix interface. Semin. Cell Dev. Biol. *71*, 75–83. https://doi.org/10.1016/j.semcdb.2017.07.027.
7. Huse, M. (2017). Mechanical forces in the immune system. Nat. Rev. Immunol. *17*, 679–690. https://doi.org/10.1038/nri.2017.74.
8. Wang, N. (2017). Review of cellular mechanotransduction. J. Phys. D Appl. Phys. *50*, 233002. https://doi.org/10.1088/1361-6463/aa6e18.
9. Martino, F., Perestrelo, A.R., Vinarský, V., Pagliari, S., and Forte, G. (2018). Cellular mechanotransduction: from tension to function. Front. Physiol. *9*, 824. https://doi.org/10.3389/fphys.2018.00824.
10. Kechagia, J.Z., Ivaska, J., and Roca-Cusachs, P. (2019). Integrins as biomechanical sensors of the microenvironment. Nat. Rev. Mol. Cell Biol. *20*, 457–473. https://doi.org/10.1038/s41580-019-0134-2.
11. Zhu, C., Chen, W., Lou, J., Rittase, W., and Li, K. (2019). Mechanosensing through immunoreceptors. Nat. Immunol. *20*, 1269–1278. https://doi.org/10.1038/s41590-019-0491-1.
12. Sun, Z., Costell, M., and Fässler, R. (2019). Integrin activation by talin, kindlin and mechanical forces. Nat. Cell Biol. *21*, 25–31. https://doi.org/10.1038/s41556-018-0234-9.
13. Ley, K., Laudanna, C., Cybulsky, M.I., and Nourshargh, S. (2007). Getting to the site of inflammation: the leukocyte adhesion cascade updated. Nat. Rev. Immunol. *7*, 678–689. https://doi.org/10.1038/nri2156.
14. Schmid-Schönbein, G.W., Sung, K.L., Tözeren, H., Skalak, R., and Chien, S. (1981). Passive mechanical properties of human leukocytes. Biophys. J. *36*, 243–256. https://doi.org/10.1016/S0006-3495(81)84726-1.
15. Nourshargh, S., and Alon, R. (2014). Leukocyte migration into inflamed tissues. Immunity *41*, 694–707. https://doi.org/10.1016/j.immuni.2014.10.008.
16. Vestweber, D. (2015). How leukocytes cross the vascular endothelium. Nat. Rev. Immunol. *15*, 692–704. https://doi.org/10.1038/nri3908.
17. Salvermoser, M., Begandt, D., Alon, R., and Walzog, B. (2018). Nuclear deformation during neutrophil migration at sites of inflammation. Front. Immunol. *9*, 2680. https://doi.org/10.3389/fimmu.2018.02680.
18. Baumgart, T., Hammond, A.T., Sengupta, P., Hess, S.T., Holowka, D.A., Baird, B.A., and Webb, W.W. (2007). Large-scale fluid/fluid phase separation of proteins and lipids in giant plasma membrane vesicles. Proc. Natl. Acad. Sci. USA *104*, 3165–3170. https://doi.org/10.1073/pnas.0611357104.
19. Lingwood, D., and Simons, K. (2010). Lipid rafts as a membrane-organizing principle. Science *327*, 46–50. https://doi.org/10.1126/science.1174621.
20. Staubach, S., and Hanisch, F.G. (2011). Lipid rafts: signaling and sorting platforms of cells and their roles in cancer. Expert Rev. Proteomics *8*, 263–277. https://doi.org/10.1586/epr.11.2.
21. Levental, I. (2020). Lipid rafts come of age. Nat. Rev. Mol. Cell Biol. *21*, 420. https://doi.org/10.1038/s41580-020-0252-x.
22. Varshney, P., Yadav, V., and Saini, N. (2016). Lipid rafts in immune signalling: current progress and future perspective. Immunology *149*, 13–24. https://doi.org/10.1111/imm.12617.
23. Tskhovrebova, L., and Trinick, J. (2003). Titin: properties and family relationships. Nat. Rev. Mol. Cell Biol. *4*, 679–689. https://doi.org/10.1038/nrm1198.
24. Granzier, H.L., and Labeit, S. (2004). The giant protein titin: a major player in myocardial mechanics, signaling, and disease. Circ. Res. *94*, 284–295. https://doi.org/10.1161/01.RES.0000117769.88862.F8.
25. Linke, W.A., and Hamdani, N. (2014). Gigantic business: titin properties and function through thick and thin. Circ. Res. *114*, 1052–1068. https://doi.org/10.1161/CIRCRESAHA.114.301286.
26. Gigli, M., Begay, R.L., Morea, G., Graw, S.L., Sinagra, G., Taylor, M.R.G., Granzier, H., and Mestroni, L. (2016). A review of the giant protein titin in clinical molecular diagnostics of cardiomyopathies. Front. Cardiovasc. Med. *3*, 21. https://doi.org/10.3389/fcvm.2016.00021.
27. Scardoni, G., Petterlini, M., and Laudanna, C. (2009). Analyzing biological network parameters with CentiScaPe. Bioinformatics *25*, 2857–2859. https://doi.org/10.1093/bioinformatics/btp517.

28. Estrada, E. (2010). Generalized walks-based centrality measures for complex biological networks. J. Theor. Biol. *263*, 556–565. https://doi.org/10.1016/j.jtbi.2010.01.014.

29. Jalili, M., Salehzadeh-Yazdi, A., Gupta, S., Wolkenhauer, O., Yaghmaie, M., Resendis-Antonio, O., and Alimoghaddam, K. (2016). Evolution of centrality measurements for the detection of essential proteins in biological networks. Front. Physiol. *7*, 375. https://doi.org/10.3389/fphys.2016.00375.

30. Qin, C., Sun, Y., and Dong, Y. (2017). A new computational strategy for identifying essential proteins based on network topological properties and biological information. PLoS One *12*, e0182031. https://doi.org/10.1371/journal.pone.0182031.

31. Ashtiani, M., Salehzadeh-Yazdi, A., Razaghi-Moghadam, Z., Hennig, H., Wolkenhauer, O., Mirzaie, M., and Jafari, M. (2018). A systematic survey of centrality measures for protein-protein interaction networks. BMC Syst. Biol. *12*, 80. https://doi.org/10.1186/s12918-018-0598-2.

32. Wiśniewski, J.R., Hein, M.Y., Cox, J., and Mann, M. (2014). A "proteomic ruler" for protein copy number and concentration estimation without spike-in standards. Mol. Cell. Proteomics *13*, 3497–3506. https://doi.org/10.1074/mcp.M113.037309.

33. Orsburn, B.C. (2021). Evaluation of the sensitivity of proteomics methods using the absolute copy number of proteins in a single cell as a metric. Proteomes *9*, 34. https://doi.org/10.3390/proteomes9030034.

34. von Andrian, U.H., Hasslen, S.R., Nelson, R.D., Erlandsen, S.L., and Butcher, E.C. (1995). A central role for microvillous receptor presentation in leukocyte adhesion under flow. Cell *82*, 989–999. https://doi.org/10.1016/0092-8674(95)90278-3.

35. Brown, M.J., Nijhara, R., Hallam, J.A., Gignac, M., Yamada, K.M., Erlandsen, S.L., Delon, J., Kruhlak, M., and Shaw, S. (2003). Chemokine stimulation of human peripheral blood T lymphocytes induces rapid dephosphorylation of ERM proteins, which facilitates loss of microvilli and polarization. Blood *102*, 3890–3899. https://doi.org/10.1182/blood-2002-12-3807.

36. Nijhara, R., van Hennik, P.B., Gignac, M.L., Kruhlak, M.J., Hordijk, P.L., Delon, J., and Shaw, S. (2004). Rac1 mediates collapse of microvilli on chemokine-activated T lymphocytes. J. Immunol. *173*, 4985–4993. https://doi.org/10.4049/jimmunol.173.8.4985.

37. Linke, W.A. (2008). Sense and stretchability: the role of titin and titin-associated proteins in myocardial stress-sensing and mechanical dysfunction. Cardiovasc. Res. *77*, 637–648. https://doi.org/10.1016/j.cardiores.2007.03.029.

38. Rushdi, M., Li, K., Yuan, Z., Travaglino, S., Grakoui, A., and Zhu, C. (2020). Mechanotransduction in T Cell development, differentiation and function. Cells *9*. https://doi.org/10.3390/cells9020364.

39. Python, J.L., Wilson, K.O., Snook, J.H., Guo, B., and Guilford, W.H. (2010). The viscoelastic properties of microvilli are dependent upon the cell-surface molecule. Biochem. Biophys. Res. Commun. *397*, 621–625. https://doi.org/10.1016/j.bbrc.2010.06.012.

40. Janmey, P.A., Fletcher, D.A., and Reinhart-King, C.A. (2020). Stiffness sensing by cells. Physiol. Rev. *100*, 695–724. https://doi.org/10.1152/physrev.00013.2019.

41. Kameritsch, P., and Renkawitz, J. (2020). Principles of leukocyte migration strategies. Trends Cell Biol. *30*, 818–832. https://doi.org/10.1016/j.tcb.2020.06.007.

42. Raynaud, F., Fernandez, E., Coulis, G., Aubry, L., Vignon, X., Bleimling, N., Gautel, M., Benyamin, Y., and Ouali, A. (2005). Calpain 1-titin interactions concentrate calpain 1 in the Z-band edges and in the N2-line region within the skeletal myofibril. FEBS J. *272*, 2578–2590. https://doi.org/10.1111/j.1742-4658.2005.04683.x.

43. Dixit, N., and Simon, S.I. (2012). Chemokines, selectins and intracellular calcium flux: temporal and spatial cues for leukocyte arrest. Front. Immunol. *3*, 188. https://doi.org/10.3389/fimmu.2012.00188.

44. Hyduk, S.J., Chan, J.R., Duffy, S.T., Chen, M., Peterson, M.D., Waddell, T.K., Digby, G.C., Szaszi, K., Kapus, A., and Cybulsky, M.I. (2007). Phospholipase C, calcium, and calmodulin are critical for alpha4beta1 integrin affinity up-regulation and monocyte arrest triggered by chemoattractants. Blood *109*, 176–184. https://doi.org/10.1182/blood-2006-01-029199.

45. Vaeth, M., Kahlfuss, S., and Feske, S. (2020). CRAC channels and calcium signaling in T cell-mediated immunity. Trends Immunol. *41*, 878–901. https://doi.org/10.1016/j.it.2020.06.012.

46. Svensson, L., McDowall, A., Giles, K.M., Stanley, P., Feske, S., and Hogg, N. (2010). Calpain 2 controls turnover of LFA-1 adhesions on migrating T lymphocytes. PLoS One *5*, e15090. https://doi.org/10.1371/journal.pone.0015090.

47. Kumar, A., Mazzanti, M., Mistrik, M., Kosar, M., Beznoussenko, G.V., Mironov, A.A., Garrè, M., Parazzoli, D., Shivashankar, G.V., Scita, G., et al. (2014). ATR mediates a checkpoint at the nuclear envelope in response to mechanical stress. Cell *158*, 633–646. https://doi.org/10.1016/j.cell.2014.05.046.

48. Gavina, M., Belicchi, M., Rossi, B., Ottoboni, L., Colombo, F., Meregalli, M., Battistelli, M., Forzenigo, L., Biondetti, P., Pisati, F., et al. (2006). VCAM-1 expression on dystrophic muscle vessels has a critical role in the recruitment of human blood-derived CD133+ stem cells after intra-arterial transplantation. Blood *108*, 2857–2866. https://doi.org/10.1182/blood-2006-04-018564.

49. Torrente, Y., Camirand, G., Pisati, F., Belicchi, M., Rossi, B., Colombo, F., El Fahime, M., Caron, N.J., Issekutz, A.C., Constantin, G., et al. (2003). Identification of a putative pathway for the muscle homing of stem cells in a muscular dystrophy model. J. Cell Biol. *162*, 511–520. https://doi.org/10.1083/jcb.200210006.

50. Torrente, Y., Tremblay, J.P., Pisati, F., Belicchi, M., Rossi, B., Sironi, M., Fortunato, F., El Fahime, M., D'Angelo, M.G., Caron, N.J., et al. (2001). Intraarterial injection of muscle-derived CD34(+)Sca-1(+) stem cells restores dystrophin in mdx mice. J. Cell Biol. *152*, 335–348. https://doi.org/10.1083/jcb.152.2.335.

51. Sauer, F., Vahokoski, J., Song, Y.H., and Wilmanns, M. (2010). Molecular basis of the head-to-tail assembly of giant muscle proteins obscurin-like 1 and titin. EMBO Rep. *11*, 534–540. https://doi.org/10.1038/embor.2010.65.

52. Graham, D.M., Andersen, T., Sharek, L., Uzer, G., Rothenberg, K., Hoffman, B.D., Rubin, J., Balland, M., Bear, J.E., and Burridge, K. (2018). Enucleated cells reveal differential roles of the nucleus in cell migration, polarity, and mechanotransduction. J. Cell Biol. *217*, 895–914. https://doi.org/10.1083/jcb.201706097.

53. Trinick, J. (1996). Titin as a scaffold and spring. Cytoskeleton. Curr. Biol. *6*, 258–260. https://doi.org/10.1016/s0960-9822(02)00472-4.

54. Astier, C., Raynaud, F., Lebart, M.C., Roustan, C., and Benyamin, Y. (1998). Binding of a native titin fragment to actin is regulated by PIP2. FEBS Lett. *429*, 95–98. https://doi.org/10.1016/s0014-5793(98)00572-9.

55. Cebecauer, M. (2021). Role of lipids in morphogenesis of T-cell microvilli. Front. Immunol. *12*, 613591. https://doi.org/10.3389/fimmu.2021.613591.

56. Toffali, L., Montresor, A., Mirenda, M., Scita, G., and Laudanna, C. (2017). SOS1, ARHGEF1, and DOCK2 rho-GEFs mediate JAK-dependent LFA-1 activation by chemokines. J. Immunol. *198*, 708–717. https://doi.org/10.4049/jimmunol.1600933.

57. Montresor, A., Bolomini-Vittori, M., Toffali, L., Rossi, B., Constantin, G., and Laudanna, C. (2013). JAK tyrosine kinases promote hierarchical activation of Rho and Rap modules of integrin activation. J. Cell Biol. *203*, 1003–1019. https://doi.org/10.1083/jcb.201303067.

58. Montresor, A., Toffali, L., Rigo, A., Ferrarini, I., Vinante, F., and Laudanna, C. (2018). CXCR4- and BCR-triggered integrin activation in B-cell chronic lymphocytic leukemia cells depends on JAK2-activated Bruton's tyrosine kinase. Oncotarget *9*, 35123–35140. https://doi.org/10.18632/oncotarget.26212.

59. Wolf, T., Jin, W., Zoppi, G., Vogel, I.A., Akhmedov, M., Bleck, C.K.E., Beltraminelli, T., Rieckmann, J.C., Ramirez, N.J., Benevento, M., et al. (2020). Dynamics in protein translation sustaining T cell preparedness. Nat. Immunol. *21*, 927–937. https://doi.org/10.1038/s41590-020-0714-5.

60. Marchingo, J.M., and Cantrell, D.A. (2020). The active inner life of naive T cells. Nat. Immunol. *21*, 827–828. https://doi.org/10.1038/s41590-020-0726-1.

61. Merkley, S.D., Chock, C.J., Yang, X.O., Harris, J., and Castillo, E.F. (2018). Modulating T cell responses via autophagy: the intrinsic influence controlling the function of both antigen-presenting cells and T cells. Front. Immunol. *9*, 2914. https://doi.org/10.3389/fimmu.2018.02914.

62. Cheng, S.Y., Wang, S.C., Lei, M., Wang, Z., and Xiong, K. (2018). Regulatory role of calpain in neuronal death. Neural Regen. Res. *13*, 556–562. https://doi.org/10.4103/1673-5374.228762.

63. Kaminskyy, V., and Zhivotovsky, B. (2012). Proteases in autophagy. Biochim. Biophys. Acta *1824*, 44–50. https://doi.org/10.1016/j.bbapap.2011.05.013.

64. Brown, M.J., Hallam, J.A., Colucci-Guyon, E., and Shaw, S. (2001). Rigidity of circulating lymphocytes is primarily conferred by vimentin intermediate filaments. J. Immunol. *166*, 6640–6646. https://doi.org/10.4049/jimmunol.166.11.6640.

65. Patteson, A.E., Vahabikashi, A., Pogoda, K., Adam, S.A., Mandal, K., Kittisopikul, M., Sivagurunathan, S., Goldman, A., Goldman, R.D., and Janmey, P.A. (2019). Vimentin protects cells against nuclear rupture and DNA damage during migration. J. Cell Biol. *218*, 4079–4092. https://doi.org/10.1083/jcb.201902046.

66. Hamouda, M.S., Labouesse, C., and Chalut, K.J. (2020). Nuclear mechanotransduction in stem cells. Curr. Opin. Cell Biol. *64*, 97–104. https://doi.org/10.1016/j.ceb.2020.05.005.

67. Makarov, A.A., Zou, J., Houston, D.R., Spanos, C., Solovyova, A.S., Cardenal-Peralta, C., Rappsilber, J., and Schirmer, E.C. (2019). Lamin A molecular compression and sliding as mechanisms behind nucleoskeleton elasticity. Nat. Commun. *10*, 3056. https://doi.org/10.1038/s41467-019-11063-6.

68. Donnaloja, F., Carnevali, F., Jacchetti, E., and Raimondi, M.T. (2020). Lamin A/C mechanotransduction in laminopathies. Cells *9*. https://doi.org/10.3390/cells9051306.

69. Yi, J.C., and Samelson, L.E. (2016). Microvilli set the stage for T-cell activation. Proc. Natl. Acad. Sci. USA *113*, 11061–11062. https://doi.org/10.1073/pnas.1613832113.

70. Machado, C., and Andrew, D.J. (2000). D-Titin: a giant protein with dual roles in chromosomes and muscles. J. Cell Biol. *151*, 639–652. https://doi.org/10.1083/jcb.151.3.639.

71. Zastrow, M.S., Flaherty, D.B., Benian, G.M., and Wilson, K.L. (2006). Nuclear titin interacts with A- and B-type lamins in vitro and in vivo. J. Cell Sci. *119*, 239–249. https://doi.org/10.1242/jcs.02728.

72. Mikelsaar, A.V., Sünter, A., Mikelsaar, R., Toomik, P., Kõiveer, A., Mikelsaar, I., and Juronen, E. (2012). Epitope of titin A-band-specific monoclonal antibody Tit1 5 H1.1 is highly conserved in several Fn3 domains of the titin molecule. Centriole staining in human, mouse and zebrafish cells. Cell Div. *7*, 21, Artn 21. https://doi.org/10.1186/1747-1028-7-21.

73. Hashimoto, K., Kodama, A., Sugino, M., Yobimoto, T., Honda, T., Hanashima, A., Ujihara, Y., and Mohri, S. (2018). Nuclear connectin novex-3 promotes proliferation of hypoxic foetal cardiomyocytes. Sci. Rep. *8*, 12337, ARTN 12337. https://doi.org/10.1038/s41598-018-30886-9.

74. Qi, J., Chi, L., Labeit, S., and Banes, A.J. (2008). Nuclear localization of the titin Z1Z2Zr domain and role in regulating cell proliferation. Am. J. Physiol. Cell Physiol. *295*, C975–C985. https://doi.org/10.1152/ajpcell.90619.2007.

75. Chauveau, C., Rowell, J., and Ferreiro, A. (2014). A rising titan: TTN review and mutation update. Hum. Mutat. *35*, 1046–1059. https://doi.org/10.1002/humu.22611.

76. Neiva-Sousa, M., Almeida-Coelho, J., Falcão-Pires, I., and Leite-Moreira, A.F. (2015). Titin mutations: the fall of Goliath. Heart Fail. Rev. *20*, 579–588. https://doi.org/10.1007/s10741-015-9495-6.

77. Preira, P., Forel, J.M., Robert, P., Nègre, P., Biarnes-Pelicot, M., Xeridat, F., Bongrand, P., Papazian, L., and Theodoly, O. (2016). The leukocyte-stiffening property of plasma in early acute respiratory distress syndrome (ARDS) revealed by a microfluidic single-cell study: the role of cytokines and protection with antibodies. Crit. Care *20*, 8. https://doi.org/10.1186/s13054-015-1157-5.

78. Zonneveld, R., Molema, G., and Plötz, F.B. (2016). Analyzing neutrophil morphology, mechanics, and motility in sepsis: options and challenges for novel bedside Technologies. Crit. Care Med. *44*, 218–228. https://doi.org/10.1097/CCM.0000000000001266.

79. Rosenbluth, M.J., Lam, W.A., and Fletcher, D.A. (2006). Force microscopy of nonadherent cells: a comparison of leukemia cell deformability. Biophys. J. *90*, 2994–3003. https://doi.org/10.1529/biophysj.105.067496.

80. Giammarco, S., Chiusolo, P., Piccirillo, N., Di Giovanni, A., Metafuni, E., Laurenti, L., Sica, S., and Pagano, L. (2017). Hyperleukocytosis and leukostasis: management of a medical emergency. Expert Rev. Hematol. *10*, 147–154. https://doi.org/10.1080/17474086.2017.1270754.

81. Mauri, P., Toppo, S., De Palma, A., Benazzi, L., Maiorino, M., and Ursini, F. (2010). Identification by MS/MS of disulfides produced by a functional redox transition. Methods Enzymol. *473*, 217–225. https://doi.org/10.1016/S0076-6879(10)73011-1.

82. Mauri, P., and Dehò, G. (2008). A proteomic approach to the analysis of RNA degradosome composition in Escherichia coli. Methods Enzymol. *447*, 99–117. https://doi.org/10.1016/S0076-6879(08)02206-4.

83. Zenaro, E., Rossi, B., Angiari, S., and Constantin, G. (2013). Use of imaging to study leukocyte trafficking in the central nervous system. Immunol. Cell Biol. *91*, 271–280. https://doi.org/10.1038/icb.2012.81.

STAR★METHODS

KEY RESOURCES TABLE

REAGENT or RESOURCE	SOURCE	IDENTIFIER
Antibodies		
327A mouse monoclonal antibody	Dr. Kristine Kikly, Eli Lilly and Co., Indianapolis, IN, USA	N/A
Alexa Fluor 488 goat anti-mouse	Invitrogen	Cat# A11001 RRID: AB_2534069
Alexa Fluor 488 goat anti-rabbit	Invitrogen	Cat# A11008 RRID: AB_143165
Alpha4 antibody (anti-CD49d)	BD Pharmigen	Cat# 555503 RRID: AB_395893
Anti-Actin	Sigma-Aldrich	Cat# A2066 RRID: AB_476693
Anti-CD19	BD Biosciences	Cat# 561741 RRID: AB_395813
Anti-CD3	BD Biosciences	Cat# 340440 RRID: AB_400513
Anti-CXCR4	Biolegend	Cat# 306506 RRID: AB_314612
Anti-L-Selectin (Anti-CD62L)	BD Pharmigen	Cat# 555544 RRID: AB_395928
Anti-LTTN1 T55	Custom-made by Eurogentec (Liege, Belgium	N/A
Anti-LTTN1 T75	Custom-made by Eurogentec (Liege, Belgium	N/A
Anti-LTTN2 A-Band	Custom-made by Eurogentec (Liege, Belgium)	N/A
Anti-LTTN3 A 168-170	Myomedix GmbH	N/A
Anti-LTTN3 TTN-Kin	Myomedix GmbH	N/A
Anti-Lyn polyclonal Antibody	Invitrogen	Cat# PA5-27361 RRID: AB_2544837
Anti-Moesin (Q480)	Cell Signaling Technology	Cat# 3150 RRID: AB_2266802
Anti-Mouse IgG (whole molecule)-FITC produced in goat	Sigma-Aldrich	Cat# F2012 RRID: AB_259456
Anti-Phospho-Ezrin (Thr567)/Radixin (Thr564)/Moesin (Thr558)	Cell Signaling Technology	Cat# 3141 RRID: AB_330232
Anti-PSGL-1 (Anti-CD162)	BD Pharmigen	Cat# 556055 RRID: AB_396325
Anti-Rabbit IgG (whole molecule)-PE produced in goat	Sigma-Aldrich	Cat# P9537 RRID: AB_261257
Anti-Rac1	Invitrogen	Cat# MA5-37658 RRID: AB_2897583
Anti-RhoA	Invitrogen	Cat# MA5-32262 RRID: AB_2809548
IB4 mouse monoclonal antibody (Anti-CD18)	American Type Culture Collection (ATCC)	N/A
Mouse IgG HRP-linked secondary antibody	Cytiva	Cat# NA931V RRID: AB_772210
Rabbit IgG HRP-linked secondary antibody	Cytiva	Cat# NA934V RRID: AB_772206

(*Continued on next page*)

Continued

REAGENT or RESOURCE	SOURCE	IDENTIFIER
Biological samples		
Buffy coats from human healthy donors	University of Verona Ethics Committee (Authorization number: 5626/02-02-2012)	N/A
Chemicals, peptides, and recombinant proteins		
Acridine Orange	Invitrogen	Cat# A1301
AmPure XP	Beckman Coulter	Cat# A63881
Bovine Serum Albumin	Sigma-Aldrich	Cat# A4503
Bradford Reagent 5X	Serva	Cat# 39222.02
Calpeptin	Sigma Aldrich	Cat# C8999
CellTracker™ Blue CMAC Dye	Thermo Fisher Scientific	Cat# C2110
CellTracker™ Green CMFDA Dye	Thermo Fisher Scientific	Cat# C2925
CellTracker™ Orange CMTMR Dye	Thermo Fisher Scientific	Cat# C2927
CellTracker™ Red CMTPX Dye	Thermo Fisher Scientific	Cat# C34552
Cholera Toxin B subunit	Sigma-Aldrich	Cat# C3741
Collagenase	Sigma-Aldrich	Cat# C2674
cOmplete Protease Inhibitor Cocktail	Roche	Cat# 11697498001
CXCL12	R&D Systems	Cat# 350-NS
DAPI	Invitrogen	Cat# D1306
DNase	Sigma-Aldrich	Cat# DN25
DNase I	Invitrogen	Cat# 18068015
Duplex-Specific Thermostable Nuclease	Evrogen	Cat# EA001
Ficoll Paque Plus	Cytiva	Cat# 17-1440-03
Fluoro Gel with DABCO™, Anti-Fading Mounting Medium	EMS	Cat# 17985-02
Formaldehyde	Titolchimica S.p.A	Cat# TC45600QQ
FSC 22 Clear Frozen Section Compound	Leica Biosystems	Cat# 3801480
Glutaraldehyde solution	Sigma-Aldrich	Cat# G6257
Herculase II Fusion DNA Polymerases	Agilent Technologies	Cat# 600675
Human dimeric E-selectin/Fc	R&D Systems	Cat# 724-ES
Human dimeric P-Selectin	R&D Systems	Cat# 137-PS
Human ICAM-1/Fc	R&D Systems	Cat# 720-IC
Human VCAM-1/Fc	R&D Systems	Cat# 862-VC
Immobilon Western Chemiluminescent HRP substrate	Millipore	Cat# WBKLS0500
Nimatek (ketamine)	Dechra	N/A
NP-40	BDH	Cat# 56009
Paraformaldehyde	Vetrotecnica	Cat# 119234431
Percoll	Cytiva	Cat# 17089101
Phalloidin Alexa Fluor™ 488	Thermo Fisher Scientific	Cat# A12379
RNaseOU Recombinant Ribonuclease Inhibitor	Invitrogen	Cat# 10777019

(*Continued on next page*)

Continued

REAGENT or RESOURCE	SOURCE	IDENTIFIER
Saponin	Sigma-Aldrich	Cat# S4521
SiR-actin	Spirochrome	Cat# SC001
SuperScrip III Reverse Transcriptase	Invitrogen	Cat# 18080044
Triton X-100	Sigma-Aldrich	Cat#T8787
Xylazine	Sigma-Aldrich	Cat# X1251
Critical commercial assays		
Human T cell Nucleofector Kit	Lonza	Cat# VPA-1002
Hyb Buffer	Evrogen	Cat# EA002
KAPA Library Quantification Kit	Kapa Biosystem	Cat# 07960140001
Qubit RNA BR Assay Kit	Thermo Fischer Scientific	Cat# Q10211
Rac1 G-LISA activation assay Kit	Cytoskeleton	Cat# BK128
Rap1 Activation Assay Kit	Millipore	Cat# 17-321
RhoA G-LISA activation assay Kit	Cytoskeleton	Cat# BK124
RNA 6000 Nano Kit	Agilent Technologies	Cat# 5067-1511
RNase Free DNase I set	Qiagen	Cat# 79254
RNeasy Mini Kit	Qiagen	Cat# 74104
TruSeq Stranded Total RNA Kit	Illumina	Cat# 20020596
Vybrant Dye Cycle Violet/SYTOX AADvanced Apoptosis Kit	Thermo Fisher Scientific	Cat# A35135
Deposited data		
Mud-PIT spectra data	This Manuscript	ftp://MSV0000873 38@massive.ucsd. edu
RNA sequencing data	This Manuscript	NCBI SRA repository under BioProject ID PRJNA701009
Experimental models: Organisms/strains		
C57BL/6J	The Jackson Laboratories	Stock# 000664 Black 6
Oligonucleotides		
Primer1 Fwd 5′-ATGAGCAATGGAGACCTAACAG-3′	This Manuscript	N/A
Primer1 Rev 5′- CCGAAGCCAAAGTCAAGATCC-3′	This Manuscript	N/A
Primer2 Fwd 5′- TGATTTCTGGAGACCCACCGA-3′	This Manuscript	N/A
Primer2 Rev 5′- CAGTTCTCAAAGTAGGCAAAGG-3′	This Manuscript	N/A
Primer3 Fwd 5′-CAGGTTCCTTCTTAGGCACAG-3′	This Manuscript	N/A
Primer3 Rev 5′- GAGGTGTCAGTCACAGTCCC-3′	This Manuscript	N/A
Primer4 Fwd 5′-GCTTCTTAACAGTTGGGACCT-3′	This Manuscript	N/A
Primer4 Rev 5′- AAGCTGTTTCAGTACAACGGG-3′	This Manuscript	N/A
Primer5 Fwd 5′-TGATCTTCTTGGGCTCTTCAG-3′	This Manuscript	N/A
Primer5 Rev 5′-AACCAGAGAAGCCTATCCCT-3′	This Manuscript	N/A
Primer6 Fwd 5′-GTACATCTCTGTGTCTTCAGAAA-3′	This Manuscript	N/A
Primer6 Rev 5′-CACCCGAAGTACCCAAGAAA-3′	This Manuscript	N/A
Primer7 Fwd 5′-GCAGCCTCTTCCTTAGGTGC-3′	This Manuscript	N/A
Primer7 Rev 5′- CAAACCACCTCCTGTGGAACC-3′	This Manuscript	N/A
Primer8 Fwd 5′- GAGATGTTGGAGGACCTAGTG-3′	This Manuscript	N/A
Primer8 Rev 5′- GAGACAACCAATAGAGACTGAG-3′	This Manuscript	N/A
Primer9 Fwd 5′- CAGCAAAGAACCAGGAAGCAG-3′	This Manuscript	N/A
Primer9 Rev 5′-CAAGACCTCAGAGTGTTGCC-3′	This Manuscript	N/A
Primer10 Fwd 5′- GTTCTACCACATAACCACTCAG-3′	This Manuscript	N/A
Primer10 Rev 5′- CTAAATTAACCATCCGTGAAACC-3′	This Manuscript	N/A

(*Continued on next page*)

Continued

REAGENT or RESOURCE	SOURCE	IDENTIFIER
Primer11 Fwd 5′- CGTCCAATTCAGGTGGTTCCC-3′	This Manuscript	N/A
Primer11 Rev 5′- CAAGACCTCAGAGTGTTGCC-3′	This Manuscript	N/A
Primer12 Fwd 5′-CTGCTGCGACACTCTATGAC-3′	This Manuscript	N/A
Primer12 Rev 5′-CTAAATTAACCATCCGTGAAACC-3′	This Manuscript	N/A
Primer13 Fwd 5′-AGCCTGTGACTTTAGATCCTC-3′	This Manuscript	N/A
Primer13 Rev 5′-CGTCCTTCCAAACCCATCGT-3′	This Manuscript	N/A
Primer14 Fwd 5′- TAGGCGGAATTCGAAGGACCA-3′	This Manuscript	N/A
Primer14 Rev 5′- CAAATGTCAGCATAAGCCGCTC-3′	This Manuscript	N/A
Primer15 Fwd 5′-TGACCAACTGGTAAATCATCCAC-3′	This Manuscript	N/A
Primer15 Rev 5′-CCTCCTGACCCATCAAGTCC-3′	This Manuscript	N/A
Primer16 Fwd 5′-TTGACAGGTCTAACACTTTCTAG-3′	This Manuscript	N/A
Primer16 Rev 5′-GCCTCTGACATCACATCCTG-3′	This Manuscript	N/A
Primer17 Fwd 5′- CTAGGCACTTTCAGTATCTCCA-3′	This Manuscript	N/A
Primer17 Rev 5′-GGCCTCTGACATCACATCCT-3′	This Manuscript	N/A
ON-TARGETplus Non-targeting Pool	Horizon/Dharmacon	Cat# D-001810-50
Custom siRNAs (ON-TARGETplus SMARTpool) for LTTN1 Seq1: Sense: 5′ G.U.G.G.A.G.A.C.A.U.U.A. C.A.U.A.U.U.A.U.U 3′	Horizon/Dharmacon	Cat# CTM-769725
Custom siRNAs (ON-TARGETplus SMARTpool) for LTTN1 Seq1: Antisense: 5′ P.U.A.A.U.A.U.G.U.A.A.U.G.U.C. U.C.C.A.C.U.U 3′	Horizon/Dharmacon	Cat# CTM-769725
Custom siRNAs (ON-TARGETplus SMARTpool) for LTTN1 Seq2: Sense: 5′ G.G.U.A.C.U.C.A.A.U.C. A.C.U.A.A.U.U.A.U.U 3′	Horizon/Dharmacon	Cat# CTM-769726
Custom siRNAs (ON-TARGETplus SMARTpool) for LTTN1 Seq2: Antisense: 5′ P.U.A.A.U.U.A.G.U.G.A.U.U.G. A.G.U.A.C.C.U.U 3′	Horizon/Dharmacon	Cat# CTM-769726
Custom siRNAs (ON-TARGETplus SMARTpool) for LTTN1 Seq3: Sense: 5′ G.A.A.U.U.G.A.U.G.U.C.C.U.G. U.G.G.A.A.U.U3′	Horizon/Dharmacon	Cat# CTM-769727
Custom siRNAs (ON-TARGETplus SMARTpool) for LTTN1 Seq3: Antisense: 5′ P.U.U.C.C.A.C.A.G.G.A. C.A.U.C.A.A.U.U.C.U.U3′	Horizon/Dharmacon	Cat# CTM-769727
Custom siRNAs (ON-TARGETplus SMARTpool) for LTTN1 Seq4: Sense: 5′ U.G.U.G.G.A.A.G.C.U.C.G.U.C. A.U.A.U.A.U.U3′	Horizon/Dharmacon	Cat# CTM-769728
Custom siRNAs (ON-TARGETplus SMARTpool) for LTTN1 Seq4: Antisense: 5′ P.U.A.U.A.U.G.A.C.G.A. G.C.U.U.C.C.A.C.A.U.U3′	Horizon/Dharmacon	Cat# CTM-769728

(*Continued on next page*)

Continued

REAGENT or RESOURCE	SOURCE	IDENTIFIER
Software and algorithms		
BeQuanti	embedded Vision System (eVS)	http://www.embed.dedvisionsystems.it/solutions/medical-imaging
Cytoscape Network Analysis Software	Cytoscape	https://cytoscape.org
FastQC	Babraham Bioinformatics	http://www.bioinformatics.babraham.ac.uk/projects/fastqc/RRID:SCR_014583
Fiji	ImageJ	https://ImageJ.net/s oftware/fiji/RRID:SCR_002285
FlowJo	FlowJo, LLC	https://www.flowjo.com/ RRID:SCR_008520
GraphPad Prism v9	GraphPad	RRID:SCR_002798
Quantity One Software	Bio-Rad	RRID:SCR_014280
Scythe software	Scythe	https://github.com/vsbuffalo/scythe
SEQUEST algorithm	University of Washington	N/A
Sickle software	Buffalo	https://github.com/vsbuffalo/sickle RRID:SCR_006800
StringTie software v1.3.3b	StringTie (CCB)	http://ccb.jhu.edu/s oftware/stringtie RRID:SCR_016323
TopHat v2.1.1 software	TopHat	https://tophat.com RRID:SCR013035
Zeiss ZEN	Carlo Zeiss	N/A
Other		
Agilent 4200 TapeStation System	Agilent	N/A
Agilent Bioanalyzer	Agilent Technologies	N/A
Axio Examiner A1 Microscope	Carl Zeiss	N/A
Axio Imager Z.2	Carl Zeiss	N/A
Axio Observer 7 Inverted Microscope	Carl Zeiss	N/A
Bioflux 200 System	Fluxion Biosciences	N/A
Blue Pippin	SageScience	N/A
Cell Culture Inserts (Transwell)	Falcon Corning	Cat# 353096
CPD 030	Balzers	N/A
Custom Microfluidic Chip	Dolomite Microfluidics	N/A
FEI/Philips XL-30 Field Emission ESEM	Philips/FEI	N/A
ImageQuant LAS 4000	GE Healthcare	N/A
Ion Trap LTQ Mass Spectrometer	Thermo	N/A
Ion-exchange chromatography	Biobasic-SCX column ThermoHypersil	N/A
MACSQuant Analyzer 10	Miltenyi Biotech	N/A
MED 010	Balzers	N/A
NanoDrop 2000 Spectrophotometer	Thermo Scientific	N/A
Nitrocellulose Western blotting membranes	Amersham GE Healthcare	Cat# 10600002
NovaSeq5000/6000	Illumina	N/A
Nucleofector 2b Device	Lonza	Cat# AAB-1001
Olympus IX50 Inverted Fluorescence Microscope	Olympus	N/A
ORCA-Flash4.0 V3 Digital CMOS camera	Hamamatsu	Cat# C13440- 20CU
Reversed phase column	Biobasic-C18 ThermoHypersil	N/A
Rotatory Microtome Cryostat CM1520	Leica Biosystems	N/A

(*Continued on next page*)

Continued

REAGENT or RESOURCE	SOURCE	IDENTIFIER
Sony Alpha IV Full Frame Camera	Sony	ILCE-7M4
SP100	World Precision Instruments	N/A
StepONE Plus Real_Time PCR System	Applied Biosystems	N/A
VictorX5 Multilabel Plate Reader	Perkin Elmer	N/A

RESOURCE AVAILABILITY

Lead contact

Further information and requests for reagents may be directed to, and will be fulfilled by, the lead contact Carlo Laudanna (carlo.laudanna@univr.it)

Materials availability

All reagents generated or used in this study are available on request from the lead contact with a completed Materials Transfer Agreement. Information on reagents used in this study is available in the key resources table.

Data and code availability

- Mud-PIT spectra data are available from MassIVE database (https://massive.ucsd.edu/ProteoSAFe/static/massive.jsp), and downloadable from ftp://MSV000087338@massive.ucsd.edu. The raw RNA sequencing data are available at the NCBI SRA repository under BioProject ID PRJNA701009.
- This paper does not report original code.
- All the data supporting the findings of the article are available within the main text or supplemental information. Any additional information required to reanalyze the data reported in this paper is available from the lead contact upon request.

EXPERIMENTAL MODELS AND SUBJECT DETAILS

Mice

C57BL/6J mice (stock no. 000664 |Black 6) were purchased from the Jackson Laboratory. Female mice at 6 months of age were used in this study. Animals were housed in pathogen-free climate-controlled facilities (temperature 21 ± 1°C and humidity 50 ± 5) and were provided with food and water ad libitum. Research involving animals was authorized by the Ethical Committee from the University of Verona and by the Italian Ministry of Health, Department of Veterinary Public Health, Nutrition and Food Safety, Directorate General of Animal Health and Veterinary Medicine (authorization no. 416/2020-PR), as required by Italian legislation (D. Lgs 26/2014) as for the application of European Directive (2010/63/UE). All efforts were made to minimize the number of animals used and their suffering during the experimental procedures.

Human

Buffy coats from human healthy donors were provided by the Blood Transfusion Center of AOUI Verona. University of Verona Ethics Committee approved experimentation involving human primary cells (authorization no. 5626/02-02-2012). All blood sample donors were eighteen years old or older and in equal percentage of males and females. Informed consent was obtained from all subjects.

METHOD DETAILS

Isolation of human primary cells

Human primary T lymphocytes were isolated from whole blood of healthy donors by Ficoll and Percoll gradients. Human primary B lymphocytes were isolated from PBMCs after blood separation on Ficoll Paque Plus and purification by negative selection. The purity of T lymphocytes preparation was evaluated by flow cytometry after staining with anti-CD3 antibody (BD Biosciences) and was more than 95%. The purity of B lymphocytes preparations was checked by flow cytometry with anti-CD19 mAb (BD Bioscience) and was more than 95%. Isolated cells were kept at 37°C in standard adhesion buffer (PBS, 1 mM $CaCl_2$, 1 mM $MgCl_2$, 10% FBS, pH 7.2) and used within 1 h.

Purification of DRM fraction

DRM (detergent resistance membrane) fractions were isolated from freshly isolated human primary T lymphocytes. Approximately 10^8 cells were washed twice in ice-cold PBS and then lysed on ice in 25 mM Tris-Hcl pH 8.0, containing 1% Tritron X-100, 150 mM NaCl, 5 mM EDTA, 1 mM Na_3VO_4, supplemented with a protease inhibitor cocktail. After homogenization through a

22-gauge needle, cells were kept on ice for 30 min and then centrifuged at 13000 rpm for 10 min at 4°C. Supernatants were mixed with an equal volume of 85% sucrose w/v in lysis buffer and a step gradient was prepared by overloading 0.7 mL of sample (42.5% sucrose/lysate) sequentially with 2.1 mL of 30% sucrose in lysis buffer followed by a top layer of 1.4 mL 5% sucrose. The gradient was centrifuged for 18 h at 200,000 × g using a Beckman SW50 rotor. Following centrifugation, 14 separate fractions (300 μL each) were collected from the top of the gradient; fractions were characterized by Western Blotting by using a polyclonal antibody anti-Lyn (Invitrogen) and by dot-blot analysis with peroxidase-conjugate cholera toxin subunit B (CTB) (Sigma-Aldrich) to detect GM1 ganglioside as raft marker. Anti-Lyn antibody and HRP-CTB were clearly able to detect best reactivity in fractions 4 to 6. Fractions 4 to 6 were then pooled and concentrated with Centricon Plus centrifugal filter devices (Millipore). The protein concentration of pooled raft fractions was evaluated with Bradford protein assay (Serva) and the protein amount was estimated as 60 μg of total raft proteins from a single preparation of 10^8 lymphocytes. Proteins in samples were, then, precipitated with TCA/acetone and resuspended in 2% Chaps buffer containing 7M urea, 2M thiourea, and DTT 100 mM. Finally, samples were dialyzed against acetonitrile and concentrated in speed-vacuum.

MUD-PIT analysis

For MUD-PIT analysis of DRM fractions and total cell lysates samples were processed as previously reported.[81] Briefly, pepsin was added at an enzyme substrate ratio of 1:100 (w/w) in 100 mM ammonium acetate, pH 2.5. After 3 h incubation at room temperature, the reaction was stopped by rapid ice cooling, and 10 mL were analyzed by MudPIT, based on two-dimensional microchromatography coupled with an ion trap mass spectrometer.[82] Peptide mixtures were first separated by means of ion-exchange chromatography (Biobasic-SCX column, 5 μm, 0.3 ID × 150 mm, ThermoHypersil) using seven steps of increasing ammonium chloride concentration (0, 50, 100, 150, 200, 300, and 600 mM). Each salt step was directly loaded onto the reversed phase column (Biobasic-C18, 0.180 ID × 100 mm, ThermoHypersil) and separated with an acetonitrile gradient: eluent A, 0.1% formic acid in water; eluent B, 0.1% formic acid in acetonitrile; the gradient profile was 5% B for 3 min followed by 5–50% B within 40 min. Eluted peptides were analyzed directly with an ion trap LTQ mass spectrometer (Thermo) and spectra were acquired in positive mode (in the range of 400–1600 m/z) using dynamic exclusion for MS/MS analysis (collision energy 35%). Computer analysis of peptide from MS/MS spectra have been performed using SEQUEST algorithm (University of Washington, USA), For the peptic peptide mixture, the ''no enzyme'' option was used. As confidence of peptide identification, the minimum values of Xcorr were greater than 1.5, 2.0, and 2.5 for single, double, and triple charge ions, respectively. Particularly, only the first-best matching peptide was taken into consideration, and only if the same peptides were found in multiple MS/MS spectra. The output data obtained from SEQUEST software were processed with the MAp roMA (Multidimensional Algorithm Protein Map) in-house algorithm allowing comparison of the protein lists, evaluation of relative abundances, and plotting virtual 2D maps.[82]

Analysis of DRM interactome

DRM protein-protein

interaction (PPI) network was reconstructed by using Cytoscape network analysis software (https://cytoscape.org). A global human interactome dataset was obtained by integrating several PPI datasets (see http://dp.univr.it/~laudanna/LCTST/styled-9/styled-30/downloads/index.html). The 82 DRM proteins identified by MS analysis were used as bioinformatic probes to extract from the global interactome a first neighbor (FN) DRM interactome. Proteins expressed in human T lymphocytes were identified by superimposing, to the DRM interactome, human primary T lymphocytes transcriptomic data sets (GSE139242; GSE112899) obtained from NCBI Gene Expression Omnibus (https://www.ncbi.nlm.nih.gov/geo/). Five topological indexes of node centrality were computed by using the Cytoscape app Centiscape[27] (see Cytoscape.sif files reported in Data S1). Statistical distribution analysis and representation to violin plots was done with GraphPad Prims 9.

RNA extraction

Total RNA was purified from human T and B lymphocytes with the RNeasy Mini Kit (Qiagen), according to the manufacturer's instructions. DNase treatment (RNase Free DNase I set, Qiagen) on column was performed. RNA quantification, purity, and integrity were assessed at NanoDrop 2000 spectrophotometer (Thermo Scientific) and by capillary electrophoresis on an Agilent Bioanalyzer (Agilent Technologies), respectively. Purified RNA was used for sequencing analysis or RT-PCR validation, as described below.

RNA sequencing and RNA-seq data processing

Whole transcriptome analysis was performed by RNA-seq technology on extracted RNA. RNA purity was measured using a NanoDrop Spectrophotometer, while RNA integrity (RNA integrity number $\geq$8.0) was assessed using RNA 6000 Nano Kit (Agilent Technologies). RNA samples were quantified using the Qubit RNA BR Assay Kit (Thermo Fisher Scientific) and RNAseq libraries were prepared from 1000 ng total RNA using the TruSeq Stranded Total RNA kit (Illumina) after ribosomal RNA depletion, according to manufacturer's instructions. The resulting RNAseq libraries were normalized with the Duplex-Specific thermostable nuclease (DSN, Evrogen) as follows. 600 ng RNAseq library was denatured at 98°C for 2 min and incubated at 68°C for 6 h in 18 μL Hyb buffer (Evrogen). 3.5 μL DSN enzyme (2U/μl) was added to the reaction and incubated at 68°C for 25 min followed by the addition of stop solution. After purification using AmPureXP beads (Beckman Coulter), libraries were enriched by PCR using primers and reaction mix provided in the Illumina RNAseq kit. After bead-based purification, the final Illumina RNAseq libraries were subjected to an additional

size-selection for 450–650 bp on a Blue Pippin (SageScience). Quality and size of libraries were assessed by capillary electrophoretic analysis with the Agilent 4200 Tape station (Agilent). Libraries were quantified by real-time PCR against a standard curve with the KAPA Library Quantification Kit (Kapa Biosystems). Libraries were then pooled at equimolar concentration and sequenced on a NovaSeq5000 or NovaSeq6000 (Illumina) analyzing on average 67 million fragments in 150PE mode for each sample. Quality of reads was assessed using FastQC software (http://www.bioinformatics.babraham.ac.uk/projects/fastqc/), and reads with more than 10% of undetermined bases or more than 50 bases with a quality score <7 were discarded. Reads were then clipped from adapter sequences using Scythe software (https://github.com/vsbuffalo/scythe), and low-quality ends (Q score <20 on a 10-nt window) were trimmed with Sickle (https://github.com/vsbuffalo/sickle). Trimmed reads were aligned to the human reference genome (GRCh38) with TopHat (version 2.1.1) with the option –library-type fr-firststrand and –b2-very-sensitive. Subsequently, reads mapping on the negative strand were selected and only read-primary alignments were retained. Transcriptome assembly of chromosome 2 was performed with StringTie software (version 1.3.3b) providing to the software the reference annotation of the TTN gene. After assembly, mapped data were visualized on the Integrative Genomics Viewer (IGV) and assembled isoforms were inspected and manually curated. To identify the coding capacity of the identified isoforms, the exons were translated using all possible frames with the web resource ExPASy (https://web.expasy.org/translate/). The search for functional protein domains in the translated isoforms were performed using the online tool InterPro (https://www.ebi.ac.uk/interpro/search/sequence/).

Analysis of LTTN isoforms expression by PCR

RNA samples were treated for 13 min at 25°C with 100 U/ml DNase I (Invitrogen) and were reverse transcribed using 5 ng/μL random primers, 1 U/μl RNase inhibitor (RNase Out, Invitrogen), and 5 U/μl reverse transcriptase (SuperScript III, Invitrogen), according to manufacturer's instruction. LTTN isoforms expression was confirmed in duplicates by PCR using Herculase II Fusion DNA Polymerase (Agilent Technologies). 20 ng RNA-equivalent cDNA were amplified with different LTTN primers (250 nM) (for sequences see key resources table, Oligonucleotides), dNTP (400 μM) buffer 1 (1x) Enzyme 0.5 U (25 μL total volume of reaction). After 1 min of initial denaturation at 95°C, DNA samples underwent 35 cycles of amplification (denaturation 95°C for 15 s, annealing 60°C for 20 s, elongation 68°C for 1 min) with a final incubation at 68°C for 4 min (StepONE Plus, Applied Biosystems). PCR products were separated by electrophoresis on 2% agarose gel and acquired by using ImageQuant Las4000 (GE Healthcare Life Science).

LTTN isoforms expression by flow cytometry

Human T lymphocytes and B lymphocytes, differently treated and/or stimulated, were fixed in formaldehyde 0.4% for 20 min at 4°C. Cells were washed and suspended in 100 μL of permeabilization buffer (PBS +5% FBS +0.5% saponin) containing TTN-specific primary antibodies, for 40 min at 4°C. After rapid wash, cells were suspended in 100 μL of permeabilization buffer containing specific secondary antibody, for 40 min at 4°C. Finally, cells were washed and suspended in ice-cold PBS. Expression quantification was by flow cytometry (MACSQuant Analyzer 10; Miltenyi Biotech). Data are shown as Mean Fluorescence Intensity (MFI) normalized to isotypic control.

Sub-cellular localization of LTTN isoforms by IF

5×10^6 T lymphocytes were fixed with formaldehyde 0.4% in PBS for 20 min at RT, washed with wash buffer (PBS+5% FBS) by microcentrifugation at 3000 RPM for 3 min, and re-suspended in 100 μL of permeabilization buffer (PBS +0.1% Triton X-100) for 7 min at 4°C. After washing as above, cells were incubated with blocking buffer (PBS +5% FBS) for 15 min at 4°C, and then TTN-specific primary antibodies were directly added and incubated for 40 min at 4°C. Cells were washed twice with wash buffer and incubated for 40 min at 4°C with secondary antibody in blocking buffer. Finally, cells were stained with 1 μg/mL DAPI for 10 min in the dark, washed, transferred to glass slides, and mounted with Fluoro Gel with DABCO, Anti-Fading Mounting Medium (EMS). Images were acquired with a wide field Zeiss AxioImager Z.2 deconvolution microscopy setting (Carlo Zeiss, Germany), equipped with Colibri 7 fluorescent LED illumination, motorized 3D scanning stage, and Hamamatsu ORCA-Flash4.0 V3 Digital CMOS camera, set at 8 bit output depth. 512x512 pixel ROIs were acquired with a 100× Plan Apochromatic oil immersion objective (AN 1.46). Each field was acquired with double fluorescent light illumination (385/30 nm ex. for DAPI and 475/36 nm ex. for Alexa Fluor 488). Automatic 3D image scanning was according to the Nyquist-Shannon sampling theorem, by using the inline ZEN 3.5 Nyquist Calculator. To achieve super resolution imaging, 3D sampling density was set at intervals of 100 nm, corresponding to about half of the calculated Nyquist sampling distance (oversampling). Oversampled 3D scans were, then, processed with Zeiss ZEN 3.5 by applying the advanced Zeiss Deconvolution (DCV) module. Image deconvolution was achieved by applying the Constrain Iterative algorithm, without auto-normalization to fully control the photon budget thus allowing full reassignment of photons from out of focus optical planes. Spectral linear unmixing was, finally, applied to remove overlapped spectral components and background noise. Deconvolved and unmixed 3D stacks were rendered and analyzed with the ZEN 3.5 Arivis 3D module. Image Ortho projections were generated with Zeiss ZEN 3.5.

LTTN1 silencing by small interfering RNA

Human T lymphocytes were plated at 5×10^6 cells/ml in RPMI, 2 mM glutamine, and 10% FBS for 2 h before silencing. Cells, suspended in nucleofector buffer at 10^7 cells/ml, were electroporated using the Nucleofector 2b Device (program U-14, Lonza; Human T cell Nucleofector Kit, Lonza) in presence of a pool of four scrambled (Horizon/Dharmacon) or four different specific LTTN1 siRNAs (ON-TARGETplus SMARTpool siRNAs, from Horizon/Dharmacon; for sequences see Key Resources Table, Oligonucleotides) according

to manufacturer's instructions. The efficiency of siRNAs nucleoporation was evaluated with fluorescein isothiocyanate-conjugated siRNAs; the efficacy of LTTN1 silencing was systematically evaluated by cytofluorimetric analysis every 24 h for 5–6 days. LTTN1-specific siRNAs were custom designed by Dharmacon service, and the target sequences were.

1) GUGGAGACAUUACAUAUUA
2) GGUACUCAAUCACUAAUUA
3) GAAUUGAUGUCCUGUGGAA
4) UGUGGAAGCUCGUCAUAUA

Evaluation of possible phenotype switch (CD45RO-CD45RA+ (naive) versus CD45RO + CD45RA- (memory)) in cells immediately before the nucleoporation (T_0) and after five days in culture, showed that T lymphocyte phenotype remained unchanged. Indeed, no difference was observed in the percentage of the distinct subsets, comparing T_0 and cultured for 5 days control, nucleoporated with scrambled siRNAs, and LTTN1-silenced T lymphocytes.

Cell viability

Human T lymphocytes were labelled for 20 min at 4°C with Vybrant DyeCycle Violet/SYTOX AADvanced Apoptosis Kit (TermoFisher Scientific) following the manufacturer's instruction. Cell viability was analyzed by flow cytometry (MACSQuant Analyzer 10; Miltenyi Biotech).

Pro-adhesive molecules expression by flow cytometry

Human T lymphocytes were labelled for 30 min at 4°C with L-Selectin-(BD), PSGL-1-(BD), CD18-(ATCC), CD49d-(BD Pharmigen), and CXCR4-specific (Biolegend) antibodies. The expression level of the molecules was analyzed by flow cytometry (MACSQuant Analyzer 10; Miltenyi Biotech). Data are shown as Mean Fluorescence Intensity (MFI) normalized to isotypic control.

Cp-ERMs and moesin expression

Human T lymphocytes, differently treated and stimulated with 0.2 μM CXCL12 (R&D Systems), were fixed in formaldehyde 0.4% for 20 min at 4°C. Cells were washed and suspended in 100 μL of permeabilization buffer (PBS +5% FBS +0.5% saponin) containing Phospho-Ezrin (Thr567)/Radixin (Thr564)/Moesin (Thr558) (Cell Signaling Technology) and Moesin (Cell Signaling Technology) specific primary antibodies, for 30 min at 4°C. After rapid wash, cells were suspended in 100 μL of permeabilization buffer containing specific secondary antibody, for 30 min at 4°C. After washing, cells were suspended in ice-cold PBS and the expression level of the molecules was analyzed by flow cytometry (MACSQuant Analyzer 10; Miltenyi Biotech). Data are shown as Mean Fluorescence Intensity (MFI) normalized to isotypic control. For Western blot, cells, treated as above, were lysed in ice-cold 1% NP-40 buffer, containing phosphatase inhibitors and complete protease inhibitor cocktail (Roche). Lysates were quantified by Bradford assay (Serva), equal amounts of proteins were subjected to 10% SDS-PAGE and blotted onto a nitrocellulose membrane (GE Healthcare). Anti-Phospho-Ezrin (Thr567)/Radixin (Thr564)/Moesin (Thr558) and anti-Moesin antibodies were used to reveal cp-ERMs and Moesin. Anti–β-actin (Sigma-Aldrich) antibody was used as loading control. Immunoreactive bands were visualized by ECL detection (Millipore) after incubation with appropriate HRP-linked secondary antibody (Cytiva), and intensities of band signals were quantified by using ImageQuant LAS 4000 (GE Healthcare).

Under-flow adhesion assay

Human T lymphocytes were suspended at 1 x 10^6/mL in standard adhesion buffer. Cell behavior in under-flow conditions was studied with the BioFlux 200 system (Fluxion Biosciences). 48-well plate microfluidics were first co-coated overnight at RT with 2.5 μg/mL human E-selectin (R&D Systems) or P-Selectin (R&D Systems). Immediately before use, microfluidic channels were washed with adhesion buffer and the assay was done at wall shear stress of 2 dyne/cm^2. The behavior of interacting cells was recorded on digital drive with a fast CCD videocamera (25 frames/s, capable of 1/2 subframe 20 ms recording) and analyzed subframe by subframe. Single areas of 0.2 mm^2 were recorded for at least 60 s. Rolling cells were automatically detected and quantified with BeQuanti (http://www.embeddedvisionsystems.it/solutions/medical-imaging).

Analysis of surface microvilli expression by SEM

Human T lymphocytes were fixed in 2% glutaraldehyde in Sorensen buffer for 2 h, postfixed in 1% osmium tetroxide in Sorensen buffer for 1 h, and dehydrated in graded acetones (Fluka). The specimens were then treated by critical point dryer (CPD 030; Balzers) and coated by gold (MED 010; Balzers), mounted on stubs, and observed in an XL 30 ESEM (FEI- Philips).

Full resolution images were imported in Zeiss ZEN 3.5 and analyzed with the Zeiss AI-based Intellesis Trainable Segmentation module, allowing machine-learning-based automatic segmentation and detection of specific image features. Intellesis training was done with analysis parameters set at "Deep Features 256", using "layer 3", with "full feature dimension". Upon Intellesis-driven image segmentation, microvilli were automatically detected and enumerated in control, round-shaped, cells by using the Zeiss ZEN Image Analysis module by applying gray values thresholding and morphological features automatically detected by Intellesis. Data were, then, expressed as average number of microvilli/cell corresponding, in our experimental setting, to 72 ± 5, calculated from the

analysis of 222 cells in 16 SEM images. This was considered the average standard. To account for morphological variability in the cell population, the analysis was normalized to definite thresholds. Thus, in nucleoporated cells, microvilli expression $\geq$90% of the average standard was scored as "full" morphology; microvilli expression ranging between 30 and 70% of standard was scored as "intermediate" morphology; microvilli expression $\leq$10% of standard was scored as "smooth" morphology, corresponding to cells almost devoid of microvilli expression. Nucleoporated cells (either with scrambled or LTTN1-specific siRNAs) from several images (3 donors) were automatically analyzed and scored according to the above procedure; data were finally expressed as % average of total analyzed cells in the three categories (full-intermediate-smooth) with SD.

Static adhesion assay

Human T lymphocytes were suspended at 3 x 10^6 cells/ml in standard adhesion buffer. Adhesion assays were done on 18-well glass slides coated with human 1 μg/mL ICAM-1 (R&D Systems) or VCAM-1 (R&D Systems) in PBS; cells, suspended in 20 μL standard adhesion buffer, were added to the wells and stimulated for 120 s at 37°C with 5 μL of CXCL12 (R&D Systems), 200 nM final concentration. After rapid washing, adherent cells were fixed in ice-cold 1.5 glutaraldehyde in PBS and counted by computer-assisted enumeration using a dedicated macro in Fiji.

Measurement of LFA-1 high-affinity state

Human T lymphocytes suspended in standard adhesion buffer at 2 x 10^6 cells/ml were stimulated for 180 s with 200 nM CXCL12 (R&D Systems) under stirring at 37°C in the presence of 327A antibody (reporter for extended conformation epitope related to a high-affinity state). After rapid washing, the cells were stained with FITC-conjugated secondary antibody (Sigma-Aldrich) and analyzed by flow cytometry (MACSQuant Analyzer 10; Miltenyi Biotech). Data are shown as Mean Fluorescence Intensity (MFI) normalized to isotypic control.

RhoA and Rac1 activation

RhoA and Rac1 activations were determined using G-LISA activation assay kits (Cytoskeleton), by adaption of the protocols as previously reported. Human T lymphocytes were stimulated or not with 200 nM CXCL12 (R&D Systems) for 120 s and were lysed for 15 min in the lysis buffer indicated in manufacturer's protocol. Protein concentrations were quantified by Precision Red (provided in the G-LISA activation assay kit). Equal amounts of proteins were added in triplicate to a 96-well plate coated with the RhoA-binding domain of rhotekin or anti-Rac1-GTP protein and incubated at 4°C for 30 min. Wells containing only lysis buffer were used as blank samples. After washing, the amount of RhoA-GTP bound or Rac1-GTP bound to each well was revealed by an anti-RhoA Ab or anti-Rac1 Ab, followed by a secondary HRP-labeled Ab and detection of HRP (provided in the G-LISA activation assay kit). Signals were measured with a microplate spectrophotometer (Victor X5 Multilabel Plate Reader, PerkinElmer) by quantifying absorbance at 490 nm.

Western blot of total RhoA and Rac1 expression

LTTN1-silenced human T lymphocytes were stimulated with 0.2 μM CXCL12 (R&D Systems) and lysed in ice-cold 1 NP-40 buffer, containing complete protease inhibitor cocktail (Roche). Lysates were quantified by Bradford assay (Serva), equal amounts of proteins were subjected to 12% SDS-PAGE and blotted onto a nitrocellulose membrane (GE Healthcare). RhoA and Rac1 were revealed by immunoblotting with anti-RhoA and anti-Rac1 primary antibodies. Anti–β-actin (Sigma-Aldrich) antibody was used for loading control. After incubation with appropriate HRP-linked secondary antibody (Cytiva), immunoreactive bands were visualized by ECL detection (Millipore) and intensities of band signals were quantified by using ImageQuant LAS 4000 (GE Healthcare).

Rap1 activation

Rap1 activation was performed by pull-down assay with RalGDS–Rapbinding domain following the manufacturer's instructions (Rap1 activation assay kit, Millipore). Human T lymphocytes were stimulated with 200 nM CXCL12 (R&D Systems) for 180 s. Cell lysates were separated by electrophoresis and blotted onto a nitrocellulose membrane (GE Healthcare). After incubation with anti-Rap1 primary antibody and HRP-coupled secondary antibodies (GEHealthcare), immunoreactive bands were visualized by ECL (EMD Millipore), acquired by using ImageQuant Las4000 (GE Healthcare Life Science) and quantified by densitometric analysis (Quantity One, Bio-Rad).

F-actin staining

Polymerization of F-actin was measured using a phalloidin binding assay (ThermoFisher Scientific). Human T lymphocytes (1 x 10^6 in adhesion buffer) were stimulated with 200 nM CXCL12 (R&D Systems) at RT. Cells were washed with ice-cold PBS and fixed with 0.4 formaldehyde for 20 min at 4°C. Cells were, then, washed and resuspended in 100 μL of permeabilization buffer (PBS +5% FBS +0.5% saponin) containing Alexa Fluor 488 Phalloidin for 60 min on ice. Cells were finally washed twice with wash buffer and analyzed by flow cytometry (MACSQuant Analyzer 10; Miltenyi Biotech).

Cell polarization assay

T lymphocytes were stained with SiR-actin_CY5 according to the manufacturer's instructions, pretreated for 30 min with 150 μg/mL calpeptin or DMSO (control) and stimulated with 200 nM CXCL12. For IF assay, upon 5 min of stimulation, cells were fixed with

formaldehyde 0.4% in PBS for 20 min at RT, washed with wash buffer (PBS+5% FBS) by microcentrifugation at 3000 RPM for 3 min, incubated with blocking buffer (PBS +5% FBS) for 15 min at RT, and then CD18-specific (ATCC) primary antibody was directly added and incubated for 40 min at RT. Cells were washed twice with wash buffer and incubated for 40 min at RT with secondary antibody in blocking buffer. Finally, cells were stained with 1 μg/mL DAPI for 10 min in the dark, washed, transferred to glass slides, and mounted with Fluoro Gel with DABCO, Anti-Fading Mounting Medium (EMS). Images were acquired with a wide field Zeiss AxioImager Z.2 deconvolution microscopy setting (Carlo Zeiss, Germany; see the "Sub-cellular localization of LTTN isoforms by IF" STAR Methods section for the acquisition method, with the addition of the Cy5 channel of excitation-emission to detect SiR-actin staining). Quantification of cell polarization in bright field images acquired at 20× magnification was done by calculating the FormCircle index of cell roundness, by using the Zeiss Zen 3.6 Image analysis module. Accordingly, with respect to polarized cells, round cells have FormCircle values closer to 1.

Chemotaxis assay

Human T lymphocyte migration assays were performed using 3 μm or 5 μm pores transwell filters (Falcon, Corning), inserted in 24-well plates. The bottom chamber was filled with 0.7 mL of RPMI +10% FBS containing 10 nM CXCL12 (R&D Systems); the top chamber was filled with 0.15 x 10^6 cells in 0.2 mL of RPMI +10% FBS. Plates were incubated for 120 min at 37°C. The inserts were, then, removed and the total number of cells migrated in the lower chamber was counted by flow cytometry (MACSQuant Analyzer 10; Miltenyi Biotech).

Deformability assay in microfluidic channels

To study human T lymphocyte deformability under flow conditions, customized microfluidic chips have been designed and fabricated in collaboration with Dolomite Microfluidics (Dolomite Microfluidics, Royston, UK). This device was developed to resemble capillary nets; a single chip consists of 48 parallel micro-channels, divided in 6 different sets of 8 channels each, with an optimized design to balance the bifurcating flow in all channels. Every single microfluidic capillary is characterized by a central restriction of 7 × 4 μm (length 250 μm) and 33 × 17 μm inlet/outlet channel sections (length 2000 μm each). Single chips have standard dimensions of 45 mm of 22.5 mm with a 3 mm quartz top layer and a 0.7 mm bottom layer (Figure S3A). To stably mount the chips on an inverted microscope and to connect the device to the flow-generating pressure pump (BioFlux pump, Fluxion), a customized 4 chips holder was designed with single inlet and outlet reservoirs dedicated to every chip (1.2 mL in volume each), allowing uniform distribution in every chip of flowing cells through the 48 microfluidics channels (Figure S3B). To better visualize cell body and nucleus resilience to deformability across channel restrictions, T lymphocytes were labelled with 0.1 mg/mL Acridine Orange for 15 min at RT, washed twice and then fluxed into the deformability device. High resolution (24 MP) images of the constriction sections were acquired with Sony Nex7 color camera plugged to an inverted epi-fluorescence microscope (Olympus IX50; images were taken at 492 nm/533 nm ex-em). Number of cells engaging the in and out sections of the microfluidic channels were enumerated with Fiji.

Hypoosmotic shock

0.5 x 10^6 human T lymphocytes were incubated with 1 mM EDTA for 10 min, washed with PBS, suspended in 300 mL NaCl 0.2% and seeded in a 24-well plate kept at 37°C. Cells were optically contrasted with DIC and 50 different images for each condition were acquired with a AxioObserver 7 inverted microscope (Carlo Zeiss, Germany) immediately after seeding and after 30 min of hypoosmotic shock. Undamaged cells were automatically detected according to Feret's diameter-based cell shape and gray level threshold detection and counted with the Zeiss ZEN 3.5 image analysis module.

Permanence of T lymphocytes in mouse circulation

Human T lymphocytes, nucleoporated with a pool of four scrambled (control) or four LTTN1-specific siRNAs, were alternatively labelled with CellTracker Orange CMTMR Dye (Thermo Fisher Scientific) or CellTracker Red CMTPX Dye (Thermo Fisher Scientific). 5 x 10^6 control and 5 x 10^6 silenced cells were mixed in a total volume of 200 μL of PBS +5% FCS and co-injected in the tail vein of adult C57BL/6J female mice. After 30 min, the animals were euthanized and, without previous perfusion, organs were immediately collected and fixed in 4% paraformaldehyde for 24 h; following, the organs were dehydrated in a sucrose 30% solution for 24 h and then embedded in Leica FSC 22 Clear compound and finally frozen. 25 μm thick serial sections of different lung lobes were cut using Leica CM1520 cryostat. Sections were seeded on gelatin-coated glass slides, stained with DAPI as nuclear marker, and mounted with DABCO mounting medium. Images were acquired with a AxioImager Z.2 wide field deconvolution upright microscopy setting (Carlo Zeiss, Germany), equipped with Colibri 7 fluorescent LED illumination, motorized 3D scanning stage and Hamamatsu ORCA-Flash 4.0 V3 Digital CMOS camera, set at 16 output bit depth. 2048x2048 pixel images were acquired with a 10× Plan Apochromatic objective (NA 0.45), corresponding to 1.33 × 1.33 mm tissue area, encompassing a tissue volume of 0.045 mm^3. Each field was acquired with triple fluorescent light illumination to detect post-fixation DAPI nuclear staining of pulmonary tissue and vital staining with CMTMR or CMTPX of injected human T lymphocytes. Spectral linear unmixing was automatically applied to all images to remove overlapped spectral components and background auto-fluorescence. Green and red artificial colors were assigned to all images to evidence LTTN1-silenced and control cells, respectively. Unmixed images were analyzed with Zeiss Intellesis AI automatic segmentation and ZEN 3.5 Image analysis modules.

Flow cytometry on mouse blood and lungs homogenates

Human T lymphocytes, nucleoporated with a pool of four scrambled (control) or four LTTN1-specific siRNAs, were alternatively labelled with CellTracker Green CMFDA (Thermo Fisher Scientific) Dye or CellTracker Blue CMAC Dye (Thermo Fisher Scientific). 3 x 10^6 control and 3 x 10^6 LTTN1-silenced cells were mixed in a total volume of 200 μL of PBS +5% FCS and co-injected in the tail vein of adult C57BL/6J female mice. After 30 min, the mouse was anesthetized, 450 μL of blood was collected from the orbital sinus and erythrocytes were allowed to sediment using 0.5% dextran. The supernatant containing the injected T lymphocytes was analyzed by flow cytometry (MACSQuant Analyzer 10; Miltenyi Biotech). After blood collection, the lungs were also collected, cut into small pieces with scissors, and put in 2 mL of freshly prepared digest solution (1 mg/mL Collagenase and 0.5 mg/mL DNase). The sample was incubated at 37°C for 60 min in shaking to allow tissue digestion. Cells were washed, resuspended in FACS buffer, filtered through a 70 μm cell strainer, and analyzed by flow cytometer (MACSQuant Analyzer 10; Miltenyi Biotech).

Intravital microscopy in muscle microcirculation

C57BL/6J mice were hosted as above and prepared according to previous studies.[48–50] Briefly, animals were anesthetized with an intraperitoneal injection of physiologic saline containing ketamine (5 mg/mL) and xylazine (1 mg/mL). For the injection of labelled cells, the right common carotid artery was cannulated with a heparinized PE-10 polyethylene catheter pointed toward the aortic arch. The skin was, then, reflected, and the pectoral muscle was bathed with saline; a coverslip (24 × 24 mm) was applied and fixed with silicon grease covering the pectoral muscle. Human T lymphocytes, nucleoporated with a pool of four scrambled (control) or four LTTN1-specific siRNAs, were labelled with Acridine Orange (AO) 0.1 μg/mL, washed twice in PBS, and directly injected in the right carotid with a digital pump (SP100; World Precision Instruments) at a flow rate of 1 μL/s. The procedure allowed the immediate arrival of labelled cells into muscle microcirculation, without previous passage in the great circulation, preventing entering other organs before imaging. Intravital imaging of striate muscle preparations was done with a AxioExaminer A1 microscope, equipped with Colibri 7 fluorescent LED illumination (Carl Zeiss, Germany). Imaging was at 5× magnification (AN 0.16) with fluorescence set at 492 nm_533/656 nm ex-em wavelengths. Digital movies were acquired with a Sony Alpha IV (ILCE-7M4) full frame (33 MP) camera allowing high resolution (4K), high framerate (50 fps) color video recording. Recorded MP4 movies were converted to AVI MJPEG and quantitative frame-by-frame analysis was done with Fiji. The image analysis field corresponded to a tissue area of about 2 mm^2. Four different behaviors of circulating cells were scored, including: a-cells that very rapidly crossed the field, with no interactions with the vascular wall; b-cells that very transiently (less than a sec.) interacted with the vascular wall; c-cells that interacted with the vascular wall, eventually with a stop-and-go and/or entrapped behavior, but with no rear leakage of cell AO labeled content; d-cells that interacted with the vascular wall, eventually with a stop-and-go and/or entrapped behavior, but manifesting a progressive rear leakage of cell AO labeled content (see Figure 7J and Video S1). In agreement with the *in vitro* analysis in microfluidics (see above), cell showing behavior (d) were scored as damaged cells and counted, along with all cells showing the other three different behaviors when crossing the imaging field. Data were expressed as % of cells manifesting behavior (d) over total cells crossing the imaging field. To calculate the hemodynamic parameters,[83] the velocity of at least 10 consecutive freely flowing cells per venule was manually measured with Fiji. Data were expressed as mean with SD (Table S4). The analysis showed no difference in the hemodynamic parameters between different animals (see Table S4). The supplemental video was edited with Apple iMovie.

QUANTIFICATION AND STATISTICAL ANALYSIS

Results are expressed as mean ± standard deviation (SD) or standard error of mean (SEM). Statistical significance was assessed by two-tailed Student's *t*-test or one-way analysis of variance (ANOVA) followed by *post hoc* Dunnett's multiple comparisons test at the 95% confidence level. Significance threshold was set at $p < 0.05$ was considered statistically significant. All statistical analyses were performed using GraphPad Prism 9 (GraphPad Software, Inc., San Diego, CA, USA).